Optimal Electrodynamic Tether Phasing and Orbit-Raising Maneuvers

Matthew S. Bitzer

Thesis submitted to the Faculty of the
Virginia Polytechnic Institute and State University
in partial fulfillment of the requirements for the degree of

Master of Science
in
Aerospace Engineering

Dr. Christopher D. Hall – Committee Chair
Dr. Craig A. Woolsey – Committee Member
Dr. Eugene M. Cliff – Committee Member

April 30, 2009
Blacksburg, Virginia

Keywords: Optimal Control, Electrodynamic Tethers, Orbit Transfers

Optimal Electrodynamic Tether Phasing and Orbit-Raising Maneuvers

Matthew S. Bitzer

(ABSTRACT)

We present optimal solutions for a point-mass electrodynamic tether (EDT) performing phasing and orbit-raising maneuvers. An EDT is a conductive tether on the order of 20 km in length and uses a Lorentz force to provide propellantless thrust. We develop the optimal equations of motion using Pontryagin's Minimum Principle. We find numerical solutions using a global, stochastic optimization method called Adaptive Simulated Annealing. The method uses Markov chains and the system's cost function to narrow down the search space. Newton's Method brings the error in the residual to below a specific tolerance. We compare the EDT solutions to similar constant-thrust solutions and investigate the patterns in the solution space. The EDT phasing maneuver has invariance properties similar to constant-thrust phasing maneuvers. Analyzing the solution space reveals that the EDT is faster at performing phasing maneuvers but slower at performing orbit-raising maneuvers than constant-thrust spacecraft. Also several bifurcation lines occur in the solution spaces for all maneuvers studied.

Acknowledgments

I would like to thank Dr. Christopher Hall for all of his advice and all of the opportunities he gave me. I became involved in research and the Aerospace and Ocean Engineering Department because of his encouragement. Those involvements evolved into Virginia Space Grant Consortium funding, graduate school funding, and countless networking opportunities throughout the vast aerospace industry in the state of Virginia.

I thank Dr. Woolsey for his advice and answering any questions I had involving controls and Dr. Cliff for helping me out with the theory behind optimal control. Another professor I would like to acknowledge is Dr. O'Brien for his career advice, his help with my other project, the Hy-V Sounding Rocket Project, and for giving me the opportunity to work in his Turbojet Lab. It really satisfied the tinkerer in me.

I would also like to thank my parents, my aunt and uncle, my Nana, and my friends. They have always supported me emotionally and financially–not only throughout my college career, but throughout my whole life. I owe so much to them.

Lastly, and most importantly, I want to thank my (almost) wife, Ali. She gives me the confidence to push myself to achieve more in life and in my career, something I did not have before I met her. I would not have made it through grad school and would not be as successful as I am now without her. Thank you.

Contents

List of Figures

List of Tables

List of Abbreviations

ASA	adaptive simulated annealing
DU	distance unit
EDT	electrodynamic tether
LEO	low-Earth Orbit
PMG	plasma motor generator
TSS	tethered satellite system
TU	time unit
STS	space transport system

Nomenclature

a	reference orbit radius
$\mathbf{B}$	magnetic field vector
B_x	x component of the magnetic field vector
B_y	y component of the magnetic field vector
B_z	z component of the magnetic field vector
$\mathbf{d}$	derivative of state vector
$\mathbf{F}$	force vector
$F : \hat{\mathbf{o}}_\mathbf{1}, \hat{\mathbf{o}}_\mathbf{2}, \hat{\mathbf{o}}_\mathbf{3}$	magnetic field frame
H	Hamiltonian
H_0	total dipole strength
I	current
$\mathbf{L}$	tether direction vector
$\hat{\mathbf{L}}$	unit tether direction vector
L_0	initial sidereal time
m	mass
$\hat{\mathbf{m}}$	dipole direction unit vector
n	dimensional mean motion at radius R_0
n_0	initial mean motion at radius r_0
$N : \hat{\mathbf{n}}_\mathbf{1}, \hat{\mathbf{n}}_\mathbf{2}, \hat{\mathbf{n}}_\mathbf{3}$	inertial coordinate frame
r	magnitude of position vector
r_0	initial orbit radius
r_1	starting orbit radius in polar system
r_2	final orbit radius in polar system
${}^{NF}\mathbf{R}$	rotation matrix
R_0	radius of attracting body in km
R_*	radius of the attracting body
$\hat{\mathbf{R}}$	position unit vector
T	dimensionless thrust
T_0	dimensionless thrust at original orbit radius
T_n	thrust component in nadir direction
T_v	thrust component in velocity direction
T_z	thrust component in $\hat{\mathbf{n}}_\mathbf{3}$ direction

u	radial velocity
v	tangential velocity
$\mathbf{V}$	velocity vector
v_x, v_y, v_z	velocity components
x, y, z	position components
α	tether length vector azimuth angle
ϵ	machine epsilon
γ	fixed dipole angle
ϕ	phase angle
$\lambda_{()}$	Lagrange costate
μ	gravitational parameter for attractive body
ν	sidereal time
θ	angular polar coordinate
ρ	tether length vector polar angle
ψ	thrust control angle
ζ	coefficient in the partial derivative of B
$\hat{\psi}$	thrust control angle with respect to local horizon
ω	rotation rate of attracting body
$\dot{()}$	inertial time derivative

Chapter 1

Introduction

The development of electrodynamic tethers (EDTs) over the past thirty years has brought to light a new and inexpensive form of Low-Earth Orbit (LEO) propulsion. An EDT is a long, conductive wire that orbits within a plasma, such as the ionosphere. The earth's magnetic field induces a current on the wire and generates thrust by means of a Lorentz force. The end bodies of the tether emit to and collect electrons from the surrounding cloud of particles to complete the circuit. When the EDT allows the magnetic field to induce a current in the wire, the tether acts as a power generator and can charge on-board batteries. However, the Lorentz force acts in the opposite direction of travel and behaves like a magnetic drag. In this mode, orbit energy is transfered into electrical energy. If the EDT supplies its own power to counter the induced current, the Lorentz force acts in the direction of travel. All thrust generated by an EDT requires no propellant. This would be the main argument for using this technology.

There are two main applications for EDTs. The first is that it can serve as a means of space debris mitigation. Every launch into orbit carries with it debris that is ejected into space. This debris poses a threat to spacecraft operating in the area.

An EDT could be attached to the debris, spent rocket stages especially, and deorbit it using the magnetic drag. With the correct control system, an independent EDT could orbit the earth, find large pieces of debris, pull it down into the atmosphere, and boost itself back up to find more debris. The second application is to boost spacecraft with decaying orbits. The most obvious example is the International Space Station. An EDT could boost the ISS using the stations power using no fuel at all, saving billions in fuel costs.

The EDT concept has been tested in three space experiments. The first experiment, TSS-1, was conducted aboard STS-46 on July 31, 1992. The main objectives were to show that a long tether could be deployed in space and to investigate and understand tether/plasma interaction. However, due to a protruding bolt in the deployment system, the tether only extended to 268 m.[2] While this was enough to prove that tethered satellites can be deployed safely to short distances and that they can gravity-gradient stabilized, the TSS-1 experiment was not able to collect any meaningful electrodynamic data.

The second TSS experiment, called TSS-1R, was a modified reflight of TSS-1 and launched with STS-75 in February 1996. The objectives for this mission were similar to those for the first: deploy the tethered satellite to a distance of 20.7 km for 20 hours and to a distance of 2.5 km for 9 hours to study space plasma physics and the system's dynamical and electrodynamical properties. This experiment, too, failed. The shuttle was only able to deploy the tether to 19.7 km before it broke, sending the tethered satellite out of the shuttle's reach. The failure was caused by excessive current being conducted by the tether, which had a potential difference of 3500 V and carried a current of 1 A. At times the voltages across the tether reached three times the predicted value.[2] The mission was seen as an expensive failure, but TSS-1R did prove that it is possible to drive a large-scale satellite with an EDT.

The third experiment, the Plasma Motor Generator (PMG) experiment, was launched as part of a Delta II second stage on June 26, 1993. The mission was designed to test how well hollow cathode tubes provided low impedance contacts to the ionosphere, study tether stability in the midst of gravity-gradient and Lorentz forces, record current and voltage readings for a full orbit, and reverse the tether current using an on-board power system. Other goals were to extend a conductive tether more than 200 m, induce a voltage over 30 V, and achieve currents of 0.1-1 A.[2] The PMG experiment achieved all of its objectives and collected over 7 hours of data. A more detailed report can be found in Ref 3.

In spite of the heavy tether activity in the mid-1990's, no further EDT experiments were conducted after TSS-1R. But the EDT concept works, and there are a couple planned EDT projects, most notably the μPET$^{\text{TM}}$by Tethers Unlimited, Inc. Having private industry develop this technology can reduce the operating costs of satellites operating in LEO because fuel is not used for station-keeping.

1.1 Motivation

There is little literature on EDT control and even less on EDT optimal control. Because literature on EDT optimal control is sparse, there are many gaps available to fill. Present optimal control research has restricted the attitude of the EDT to the nadir direction and is focused on maximizing orbit changes in a determined amount of time. It is difficult to relate the results of the literature to more well-known (and more useful) optimal orbit transfer problems–such as minimum-time, constant low-thrust maneuvers. For EDT technology to be functional and practical, it needs to be controlled efficiently. Though open-loop control is not practical, knowing the best possible trajectory for a given set of initial conditions is essential to understanding

the capabilities of an EDT.

1.2 Problem Definition

The aim of my research is to find optimal solutions to basic orbital maneuvers such as phasing, orbit-raising, and inclination change maneuvers using a point mass EDT. We assume the system can be described by the two-body problem where the only forces acting on the EDT are gravity and Lorentz forces. The initial conditions for each maneuver are the same: the spacecraft begins in a circular orbit, but the end boundary conditions are different. The phasing maneuver, a maneuver where a spacecraft must catch up or slow down to a target spacecraft in the same orbit, is a rendezvous maneuver where the orbit-raising and inclination change maneuvers just have target orbits.

Two magnetic field models will be used. The first is a non-tilted dipole model. This means that the earth's magnetic field is simulated by a magnetic dipole that is aligned with the earth's rotational axis. In this model, the magnetic field is perpendicular to the earth's equatorial plane. If the EDT is in this plane, the Lorentz forces will always be in the equatorial plane, thus creating a two-dimensional problem. There is much in the literature on 2D optimal orbital control of constant-thrust spacecraft performing phasing and orbit-raising maneuvers. The solutions for the optimal control of a constant-current EDT will be compared to these cases.

The second magnetic field model is a tilted dipole model. In reality, the earth's magnetic field is tilted with respect to the rotational axis, and there are no planes of symmetry where all of the thrust can be in the orbit plane. Therefore, the problem turns into a three-dimensional optimal control problem. Solutions for all three maneuvers in a 3D environment will be presented.

1.3 Approach

Because there is no literature on minimum-time, constant-thrust EDT optimal control, we must solve a set of twelve differential equations from scratch. First we develop the optimal equations of motion based on the two-body problem, the physics of the system, and the principles of calculus of variations. Finding the initial values of the twelve states involves a modified version of the shooting method. In the shooting method, the simulation integrates the equations of motion forward from the provided initial conditions and compares its end state to the desired state defined by the problem definition. The difference between the end state and the desired state is called the residual. Because there is such a large search space, a good search algorithm is required.

A process called simulated annealing (SA) is a wide-range search algorithm that is perfectly suited for dealing with a large search space. It mimics the physical process of taking a highly unorganized, melted material and reducing the temperature slowly so that the crystalline structure is nearly perfect. Simulated annealing involves lowering the energy state, or performance index, of the system slowly so that the algorithm can find possible global minima for the residual. As the energy state lowers, the number of possible locations for the global minima within the search space decreases until only one location remains. Once SA has reduced the search space down to one small area, the Newton-Raphson Method can reduce the residual down to a specified tolerance.

1.4 Thesis Overview

In the next chapter, we will complete a review of optimal control literature for spacecraft in general and for EDTs specifically. Several numerical solution search algorithms are also reviewed. Chapter 3 focuses on the dynamics of the system. We list what assumptions and simplifications are made, and how we use these simplifications to make a mathematical model of the dynamics. We develop the optimal control problem and optimal control laws for the two types of maneuvers in the fourth chapter, and present the solution algorithm in the fifth chapter. Finally, we present the results of our analysis in Chapter 6 and end with some concluding remarks in Chapter 7.

Chapter 2

Literature Review

In this chapter, we present a review of the optimal control literature for minimum-time constant-thrust spacecraft and EDTs. The optimal control of constant-thrust spacecraft acts as base of comparison for my optimal constant-current EDT maneuvers. We also present the numerical methods we use to find solutions to the optimal control problem.

2.1 Pontryagin's Minimum Principle

A quick search on a literature database shows that there are hundreds of journal articles, conference papers, and books on the optimal control of constant-thrust spacecraft. We focus on work that involves solving a two-point boundary value problem that arises from Pontryagin's Minimum Principle.

According to Ref. 4, Pontryagin's Minimum Principle requires the following preliminaries: a dynamical system

$$\dot{\mathbf{x}}(t) = \mathbf{f}(\mathbf{x}(t), u(t)), \qquad \mathbf{x}(0) = \mathbf{x}_0 \tag{2.1}$$

where $\mathbf{f} : \mathbb{R}^n \times \mathbb{R}^m \longmapsto \mathbb{R}^n$ is smooth, a set piecewise continuous control functions,

$$\mathbf{u}(\cdot) : [0, t_1] \longmapsto \Omega \subset \mathbb{R}^m \tag{2.2}$$

where Ω is a given closed and bounded set, a smooth target set

$$\Theta^f \equiv \{\mathbf{x} \in \mathbb{R}^n \mid \theta_i^f(\mathbf{x}) = 0,\ i = 1, ..., q\} \tag{2.3}$$

where θ_i^f are the q elements of Θ, a real-valued, scalar cost functional,

$$J(\mathbf{x}(\cdot), \mathbf{u}(\cdot)) \equiv \int_0^{t_1} f_\circ(\mathbf{x}(t), \mathbf{u}(t))dt \tag{2.4}$$

and vector of Lagrange costates, $\lambda(t)$. Define the variational Hamiltonian as

$$H = \lambda(t)^T \mathbf{f}(\mathbf{x}(t), u(t)) \mp \lambda_0 \mathbf{f}(\mathbf{x}(0), \mathbf{u}(0)) \tag{2.5}$$

Pontryagin's Minimum Principle states that if $\mathbf{x}^*$ and if $\mathbf{u}^*$ defined on $[0, t_1^*]$ are an optimal state-control pair, then there exists a real number λ_0, and an absolutely-continuous vector-valued function $\lambda(\cdot) \longmapsto \mathbb{R}^n$, such that:

1. $\lambda_0 \geq 0$ and $(\lambda_0, \lambda(t)) \neq 0 \in R^{1+n}$
2. $\dot{\lambda}(t) = -\frac{\partial H}{\partial x}^T \Big|_{x^*, u^*}$
3. $\lambda(t_1^*) \perp \Theta^1 \Big|_{x(t_1^*)}$
4. $H(\lambda_0, \lambda(t), \mathbf{x}^*(t), \mathbf{v}) \geq H(\lambda_0, \lambda(t), \mathbf{x}^*(t), \mathbf{u}^*(t)) \ \ \forall \ \ \mathbf{v} \in \Omega$
5. $H(\lambda_0, \lambda(t), \mathbf{x}^*(t), \mathbf{u}^*(t)) = 0$ for $0 \leq t \leq t_1^*$

The first condition ensures that there is not a trivial solution for the costates, the second condition gives the differential equations of the costates, the third condition

gives necessary end conditions for the costates, called transversality conditions, and the last two conditions ensure that the Hamiltonian is minimized if the state-control pair is optimal. These conditions are the necessary conditions for optimality.

2.2 Optimal Control of Constant-Thrust Spacecraft

An oft referenced text is the work of Bryson and Ho.[5] They have many examples of continuous optimal control problems–including ones with specified and unspecified final times, path and control constraints, and feedback control. The classical example that best matches our work is Zermelo's Problem,[4,5] in which an airship with constant speed must go from point A to point B through windy conditions in minimum time. The initial and final state variables are known, but the initial Lagrange costates and the final time are unknown.

There are many examples in the literature of optimal spacecraft constant-thrust maneuvers which resemble Zermelo's Problem. Wiesel and Alfano[6] present solutions to optimal orbit transfers that require many revolutions to complete. Alfano and Thorne[7] complete a series of mission planning charts for optimal circle-to-circle orbit-raising maneuvers for several propellant mass fractions. Thorne and Hall[8] develop a method for approximating the initial values of the Lagrange costates for a circle-to-circle orbit-raising maneuver. In Ref. 9, the Thorne and Hall extend their work by comparing the approximate solutions to known two-dimensional (2D) and three-dimensional (3D) examples from Ref. 5. These approximations can be used as initial guesses for the costates in a numerical solver. Thorne[10] presents 2D optimal equations of motion in Cartesian and polar coordinates and 3D optimal equations of motion in Cartesian coordinates for a spacecraft with constant thrust. Combining these works gives a comprehensive guide on how to find an optimal orbit-raising trajectory for

a point-mass spacecraft and serves as a basis for comparison for optimal constant-current EDT orbit-raising maneuvers.

2.2.1 Optimal Constant-Thrust Phasing Maneuvers

Another common orbit maneuver is the phasing maneuver. Initially, two spacecraft are in the same orbit but are separated by a phase angle. One of the spacecraft then performs a phasing maneuver to rendezvous with the other. Hall and Collazo-Perez[11] present several optimal phasing maneuvers for a wide range of thrusts and phase angles. The main conclusion in this work is that there exists a near-invariance property in the initial Lagrange costates and time of flight. If the magnitude of the thrust and the phase angle increase or decrease by an order of magnitude, the initial costates and time of flight are constant to at least two decimal places for thrusts where gravity is the dominant force in the system. Ref. 11 supports the claim by constructing locus plots of the initial costates for a fixed thrust and for varying phase angles and shows how the plots are invariant for a wide range of thrusts. The locus plots show the initial thrust direction in the phasing maneuver. In Chapter 5, we use Ref. 11 as a basis for comparison and see if EDTs have the same invariance properties.

2.3 Dynamics and Control of Electrodynamic Tethers

There is much in the literature on the dynamics and control of electrodynamic tethers. A good reference on tether dynamics is a book by Beletsky and Levin.[12] There is a chapter on EDT models that includes point mass models, rigid body models, and a limited flexibility model for EDTs in tilted and non-tilted magnetic fields. However,

like most textbooks, the examples are general, and it is up to the research community to solve more specific problems.

Tragesser and San[13] develop the equations of motion and a control algorithm for the current for a point-mass EDT aligned with the nadir direction in terms of orbit elements. Pearson et al.[14] show that when an EDT is not restricted to the local vertical, it can generate more thrust, especially at higher inclinations. They, too, develop a control algorithm and show simulations to support their conclusions.

Other work on the control of EDTs focuses on libration control. Libration control is when the control algorithm dampens oscillations in the tether. Williams et al.[15] develop a wave-absorbing control for a continuum tether model in a non-tilted magnetic field that mitigates instabilities caused by the electromagnetic forces in the EDT. The control relies on one of the tether end-bodies to be controllable. Peláez and Andrés[16] model the EDT as a rigid rod with two end masses. Using this model, EDTs do not have equilibrium positions, even in the local vertical in a circular orbit. The authors instead presented periodically stable solutions for EDTs in inclined orbits in a non-tilted dipole. Peláez and Lorenzini[17] used the work from Ref. 16 to create two libration control algorithms for EDTs in inclined orbits. The control algorithms force the system toward the periodic solutions.

All of the work above is based on restrictive assumptions that make the results hard to apply to a real world application. Ellis and Hall[18,19] developed a flexible EDT model with gyrostat end-bodies in a tilted dipole magnetic field. A gyrostat body is one that uses momentum exchange devices to control the attitude. The authors studied the uncontrolled dynamics of the system and discover that when the end-bodies are small, the EDT becomes unstable. Also, they find that higher currents in the tether perform minor orbit maneuvers better than smaller currents. The results are verified using the Method of Manufactured Solutions.[18,19]

2.3.1 Optimal Control of Electrodynamic Tethers

The literature on EDT optimal control is lacking and has much room for improvement. Williams[20] presents optimal equations of motion in terms of orbit elements and uses current as the control to perform orbit-raising maneuvers. The author assumes that the EDT always points in the nadir direction and that the magnetic dipole is not tilted. Williams uses a direct, nonlinear programming algorithm with 400 evenly spaced collocation points to solve the optimal control problem. Direct optimization methods have less sensitivity to initial guesses than indirect methods like Pontryagin's Minimum Principle, but optimality is not guaranteed.[1] Williams' solution algorithm is computationally expensive and prevents him from solving for long-duration maneuvers.

Stevens and Wiesel[21] build off of Ref. 20 and solve several long-duration maneuvers, including maximum orbit-raising, maximum inclination change, and minimum-time maneuvers, using the DIDO optimization software package. This algorithm is more efficient than Williams' method because only 40 nodes are needed to describe a 500 revolution maneuver. DIDO, however, is also a direct optimization method and requires that the operator check the Hamiltonian to verify that the solution minimizes it.

The literature on optimal EDT control is not nearly as complete as the literature on the optimal control of constant-thrust spacecraft. While Refs. 20 and 21 use flexible tether models, their magnetic dipole models are primitive; their results are specific to the earth and their choice of tether properties, and the results are not compared to the large database of existing optimal spacecraft control solutions.

2.4 Solution Search Algorithms

All of the work we mention in Section 2.2 gives a warning about the large sensitivity of the initial Lagrange costates. If the initial guess of the initial costates is not within a small radius of the solution, the numerical solver quickly diverges. Kim[1] presents a solution algorithm that combats this problem. The algorithm begins with a global, stochastic search called Adaptive Simulated Annealing (ASA). It mimics the physical process of taking a highly unorganized, melted material and reducing the temperature slowly so that the crystalline structure is nearly perfect. Simulated annealing involves lowering the energy state, or performance index, of the system slowly so that the algorithm can find possible minima. As the energy state lowers, the number of possible locations for the global minima within the search space decreases until only one location remains. Once ASA narrows down the search space to a small area containing the optimal solution, Ref. 1 uses a Newton or quasi-Newton method to reduce the error in the numerical solution to below a certain tolerance.

2.5 Summary

In this chapter, we present a review of literature covering the optimal control of constant-thrust spacecraft using indirect methods, the dynamics and control of EDTs, and of useful solution algorithms. We use this information to develop the equations of motion in Chapter 3, the optimal control laws in Chapter 4, a solution algorithm in Chapter 5, and to generate numerical solutions in Chapter 6.

Chapter 3

System Dynamics

Controlling a realistic EDT is a complex problem which no one has been able to solve. As in any engineering discipline, the actual dynamics of the system are simplified through modeling, and the problem becomes easier to solve. In this chapter, we outline the details of my simplifications to the system and the resulting equations of motion for phasing and orbit-raising maneuvers.

3.1 Electrodynamic Tether Model

The EDT is a point mass in a two-body system. The only forces acting on the tether are gravity and the Lorentz force created by the interaction of the tether with the attracting body's magnetic field. A Lorentz force for a point-mass EDT is defined as:

$$\mathbf{F} = I\mathbf{L} \times \mathbf{B} \tag{3.1}$$

where i is the current through the tether, $\mathbf{L}$ is the tether length vector, and $\mathbf{B}$ is the magnetic field vector. We assume $\|I\mathbf{L}\|$ to be constant. An EDT converts the most current into thrust by keeping the tether length vector perpendicular to the magnetic

field vector. Therefore, we also assume that $\mathbf{L} \perp \mathbf{B}$ always.

3.2 Magnetic Field Model

We use a magnetic dipole model to simulate the attracting body's magnetic field. The magnetic field vector equation for this model is:[22]

$$\mathbf{B}(\mathbf{R}) = \frac{R_*^3 H_0}{r^3} \left(3 \left(\hat{\mathbf{m}} \bullet \hat{\mathbf{R}} \right) \hat{\mathbf{R}} - \hat{\mathbf{m}} \right) \tag{3.2}$$

where R_* is the radius of the attracting body, H_0 is the total dipole strength, r is the magnitude of the position vector, and $\hat{\mathbf{R}}$ is the unit position vector, and $\hat{\mathbf{m}}$ is the unit dipole direction vector, which is parameterized as,

$$\hat{\mathbf{m}}(\nu) = \cos\gamma \hat{\mathbf{n}}_3 + \sin\gamma \left(\cos\nu \hat{\mathbf{n}}_1 + \sin\nu \hat{\mathbf{n}}_2 \right) \tag{3.3}$$

where γ is the angle between $\hat{\mathbf{n}}_3$ and $\hat{\mathbf{m}}$, and ν is the sidereal time. The dipole direction vector is fixed with respect to the attracting body so when the attracting body spins with respect to an inertial frame, the magnetic dipole spins with it. Figure 3.1 illustrates the magnetic field model.

The magnetic field is tilted when $\hat{\mathbf{m}}$ is not parallel to the spin axis of the attracting body and non-tilted when $\hat{\mathbf{m}}$ is parallel to the spin axis of the attracting body (i.e. $\gamma = 180°$). When the magnetic field is tilted, $\hat{\mathbf{m}}$ changes with time in the following way:

$$\frac{d}{dt}\hat{\mathbf{m}} = \omega \hat{\mathbf{n}}_3 \times \hat{\mathbf{m}}, \qquad \hat{\mathbf{m}}(0) = \hat{\mathbf{m}}_0 \tag{3.4}$$

where ω is the rotation rate of the attracting body. The initial dipole direction depends on the orientation of the dipole with respect to the attracting body, but

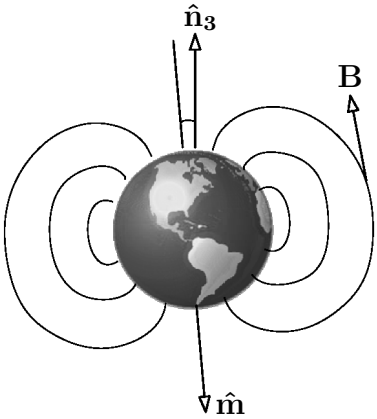

Figure 3.1: Tilted Dipole Magnetic Field Model

we set up the problem so that $\hat{\mathbf{m}}_0$ only has components in the $\hat{\mathbf{n}}_3$ and positive-$\hat{\mathbf{n}}_1$ directions.

3.3 Derivation of the 3D Equations of Motion in Cartesian Coordinates

We use the physics of the problem to develop a coordinate system and the equations of motion in Cartesian coordinates, which are useful in defining the end-point boundary conditions.

3.3.1 3D Equations of Motion

We state the equations of motion based in an inertial coordinate frame. The inertial frame is defined as $N : \hat{\mathbf{n}}_1, \hat{\mathbf{n}}_2, \hat{\mathbf{n}}_3$, where $\hat{\mathbf{n}}_1$ is in the Vernal Equinox direction, $\hat{\mathbf{n}}_3$ is parallel to the attracting body's axis of rotation, and $\hat{\mathbf{n}}_2$ is the cross product of $\hat{\mathbf{n}}_3$ and $\hat{\mathbf{n}}_1$. The equations of motion for the two-body problem with thrusting are as follows:

$$\dot{\mathbf{R}} = \mathbf{V} \tag{3.5}$$

$$\dot{\mathbf{V}} = -\frac{\mu}{r^3}\mathbf{R} + \frac{IL}{m}\hat{\mathbf{L}} \times \mathbf{B} \tag{3.6}$$

where $\mathbf{R} = [x\ y\ z]^T$ is the inertial position vector, $\mathbf{V} = [v_x\ v_y\ v_z]^T$ is the inertial position vector, $r = \sqrt{x^2 + y^2 + z^2}$, μ is the gravitational parameter for the attracting body, and $\hat{\mathbf{L}}$ is the unit tether length vector and the optimal control variable. Here, x, y, and z are components of the EDT position vector, and v_x, v_y, and v_z are the derivatives of x, y, and z with respect to the inertial frame. The remaining equation of motion is Equation 3.4, the differential equation for the magnetic dipole.

3.4 Simplifying the Cartesian Equations of Motion to Two Dimensions

Reducing the problem to two dimensions simplifies the problem greatly. We restrict EDT to an orbit in the attracting body's equatorial plane and define the magnetic field as non-tilted.

3.4.1 2D Magnetic Field Model and Coordinate System

The magnetic field vector equation in the equatorial plane of an attracting body with a non-titled magnetic dipole is

$$\mathbf{B}(\mathbf{r}) = \frac{R_* H_0}{r^3}\hat{\mathbf{n}}_\mathbf{3} \tag{3.7}$$

Because $\mathbf{B}$ is always perpendicular to the attracting body's equatorial plane, the cross product in Equation 3.6 is replaced with a scalar product.

3.4.2 2D Equations of Motion

The 2D equations of motion are based on the inertial frame, as well. A diagram of the 2D coordinate system is shown in Figure 3.2. The black circle represents the initial position of the EDT, and the lightest circle represents the initial position of the target satellite. Both satellites are in the same initial orbit and are separated by a phase angle, *phi*.

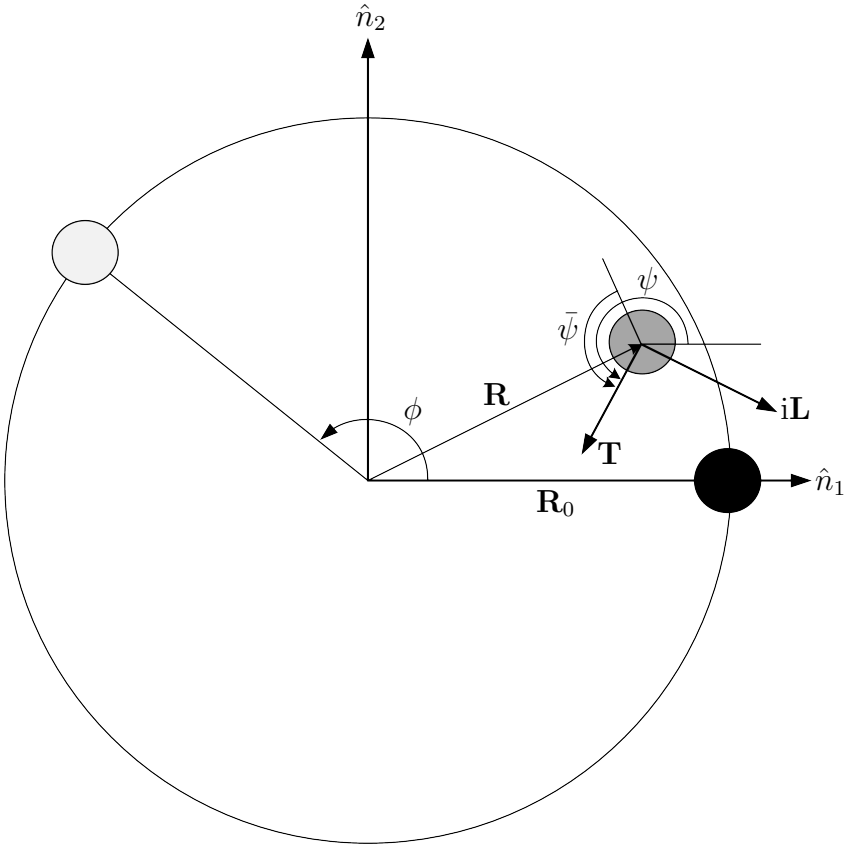

Figure 3.2: 2D Optimal Phasing Maneuver Geometry

The equations of motion for the two-dimensional, two-body problem with thrusting are as follows:

$$\dot{\mathbf{R}} = \mathbf{V} \tag{3.8}$$

$$\dot{v}_x = -\frac{\mu}{r^3}x + \frac{BIL}{m}\cos\psi \tag{3.9}$$

$$\dot{v}_y = -\frac{\mu}{r^3}y + \frac{BIL}{m}\sin\psi \tag{3.10}$$

where $\mathbf{R} = [x\ y]^T$ is the inertial position vector, $\mathbf{V} = [v_x\ v_y]^T$ is the inertial position vector, $r = \sqrt{x^2 + y^2}$, and ψ is the thrust angle.

3.5 Derivation of the 2D Equations of Motion in Polar Coordinates

Polar coordinates are convenient when solving orbit-raising problems because the end boundary condition is a circular orbit, not a point on a circular orbit as in phasing maneuvers.

3.5.1 Magnetic Field Model and Coordinate System

In this section, we use the same inertial frame as used in Section 3.4.1. A diagram of the polar coordinate system is shown in Figure 3.3. The two position variables are r, the radius of the spacecraft, and θ, the angle between r and $\hat{\mathbf{n}}_\mathbf{1}$. The magnetic field model described by Equation (3.7) applies to the 2D polar formulation as well.

3.5.2 Equations of Motion for Orbit-Raising Maneuvers

The polar equations of motion for the two-body problem with thrusting are,[9]

$$\dot{r} = u \tag{3.11}$$

$$\dot{u} = \frac{v^2}{r} - \frac{\mu}{r^2} + \frac{BIL}{m}\sin\bar{\psi} \tag{3.12}$$

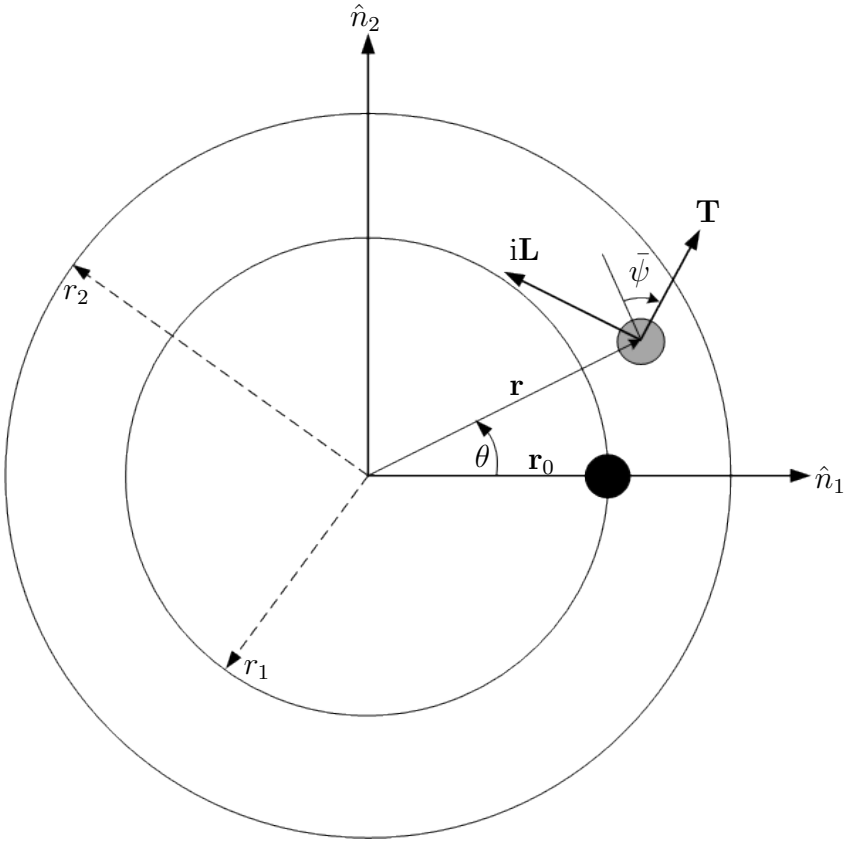

Figure 3.3: Optimal Orbit Raising Maneuver Geometry

$$\dot{v} = -\frac{uv}{r} + \frac{BIL}{m}\cos\bar{\psi} \tag{3.13}$$

where u is the radial velocity, and v is the tangential velocity.

3.6 Summary

In this chapter, we present the reference frames and equations of motion of three systems: a three-dimensional Cartesian system, a two-dimensional Cartesian system, and a two-dimensional polar system. Cartesian coordinates are convenient when solving phasing maneuver problems because they make specifying a unique end-point boundary condition easy. Polar coordinates are convenient for orbit-raising maneuvers

because the end condition is a circular orbit, not a point on a circular orbit. We use the equations of motion presented in this chapter to develop the optimal equations of motion in the next chapter.

Chapter 4

Optimal Control Problem

Formulating the optimal control problem requires a cost function and the use of Pontryagin's Minimum Principle, which provides the necessary conditions for optimality. We use the optimality conditions to transform the equations of motion in the previous chapter into minimum-time equations of motion.

4.1 Optimal Control Law and Equations of Motion for Phasing Maneuvers

In this section, we develop the optimal control laws and equations of motion for the three-dimensional and two-dimensional Cartesian systems using Pontryagin's Minimum Principle. The cost function for all three optimal control problems is the time of flight,

$$J = \int_0^{t_f} dt \tag{4.1}$$

4.1.1 Optimal 3D Equations of Motion

Using Equations (3.5), (3.6), and (3.4) and a vector of Lagrange costates, λ, the variational Hamiltonian for the three-dimensional Cartesian system is

$$H = \lambda_x v_x + \lambda_y v_y + \lambda_z v_z - \lambda_{vx}\frac{\mu}{r^3}x - \lambda_{vy}\frac{\mu}{r^3}y - \lambda_{vz}\frac{\mu}{r^3}z + \lambda_\nu \omega + \lambda_{\mathbf{v}} \bullet \mathbf{T} \tag{4.2}$$

where $\lambda_{\mathbf{v}} = \begin{bmatrix}\lambda_{v_x} & \lambda_{v_y} & \lambda_{v_z}\end{bmatrix}^T$ and $\mathbf{T}$ is the inertial acceleration vector defined as,

$$\mathbf{T} = \frac{IL}{m}\hat{\mathbf{L}} \times \mathbf{B} \tag{4.3}$$

We find the optimal control law by finding a control that minimizes the Hamiltonian, which contains acceleration terms and the only control dependent terms:

$$\lambda_{\mathbf{V}} \bullet \mathbf{T} = \frac{IL}{m}\lambda_{\mathbf{V}} \bullet (\hat{\mathbf{L}} \times \mathbf{B}) \tag{4.4}$$

The lead coefficient is positive, so the operation that minimizes the Hamiltonian is:[23]

$$\min \lambda_{\mathbf{V}} \bullet (\hat{\mathbf{L}} \times \mathbf{B}) = \min \hat{\mathbf{L}} \bullet (\mathbf{B} \times \lambda_{\mathbf{v}})$$

where $\mathbf{B}$ and $\lambda_{\mathbf{v}}$ are fixed, present-values on the extremal path. The choice of $\hat{\mathbf{L}}$ that minimizes the Hamiltonian is,[23]

$$\hat{\mathbf{L}}^* = -\frac{\mathbf{B} \times \lambda_{\mathbf{v}}}{\|\mathbf{B} \times \lambda_{\mathbf{v}}\|}, \qquad \|\mathbf{B} \times \lambda_{\mathbf{v}}\| \neq 0 \tag{4.5}$$

Equation 4.5 states, by the definition of the cross product, that $\hat{\mathbf{L}}^*$ is in a plane perpendicular to the magnetic field, as per our assumption in Chapter 3. We choose

to parameterize Equation 4.5 using two angles: a polar angle, ρ, and an azimuth angle, α.

To complete the analysis, we need six more equations to solve a system with twelve state and costate variables. The remaining equations of motion are

$$\dot{\lambda}_{\mathbf{r}} = -\frac{\partial H}{\partial \mathbf{r}}^T = \frac{\lambda_{\mathbf{v}}}{r^3} - \frac{\lambda_{\mathbf{v}} \bullet \mathbf{r}}{r^5}\mathbf{r} - \frac{R_* H_0 I L}{m}\frac{\partial \mathbf{B}}{\partial \mathbf{r}}^T \frac{\lambda_{\mathbf{v}}\left(\lambda_{\mathbf{v}} \bullet \mathbf{B}\right) - \mathbf{B}\|\lambda_{\mathbf{v}}\|^2}{\|\mathbf{B} \times \lambda_{\mathbf{v}}\|} \tag{4.6}$$

$$\dot{\lambda}_{\mathbf{v}} = -\frac{\partial H}{\partial \mathbf{v}}^T = -\lambda_{\mathbf{r}} \tag{4.7}$$

$$\dot{\lambda}_{\nu} = -\frac{\partial H}{\partial \nu} = -\left(\frac{IL}{m}\right)\left(\frac{\lambda_{\mathbf{v}}\left(\lambda_{\mathbf{v}} \bullet \mathbf{B}\right) - \mathbf{B}\|\lambda_{\mathbf{v}}\|^2}{\|\mathbf{B} \times \lambda_{\mathbf{v}}\|}\right) \bullet \frac{\partial \mathbf{B}}{\partial \nu} \tag{4.8}$$

$$\tag{4.9}$$

where

$$\frac{\partial \mathbf{B}}{\partial \mathbf{r}} = R_* H_0 \left(\frac{3}{r^5}\left(\mathbf{R}\hat{\mathbf{m}}^T + \hat{\mathbf{m}}\mathbf{R}^T + (\hat{\mathbf{m}}\mathbf{r})I_{3x3}\right) - \frac{15\mathbf{R}\mathbf{R}^T}{r^7}\right) \tag{4.10}$$

$$\frac{\partial \mathbf{B}}{\partial \nu} = \frac{R_* H_0}{r^3}\left(\left(3\hat{\mathbf{m}}'(\nu)^T\hat{\mathbf{R}}\right)\hat{\mathbf{R}} - \hat{\mathbf{m}}'(\nu)\right) \tag{4.11}$$

and where

$$\hat{\mathbf{m}}'(\nu) = \frac{\mathrm{d}\hat{\mathbf{m}}}{\mathrm{d}\nu} = \sin\theta \begin{bmatrix} -\sin\nu \\ \cos\nu \\ 0 \end{bmatrix}_N \tag{4.12}$$

Solving differential equations with as many terms as Equations (4.6–4.11) is computationally expensive. We simplify Equations (4.6) and (4.8) by setting,

$$\frac{\partial \mathbf{B}}{\partial \mathbf{r}} = \frac{\partial \mathbf{B}}{\partial \nu} = 0$$

which yields

$$\dot{\lambda}_x = \frac{\lambda_{vx}\mu}{r^3} - \frac{3\mu x}{r^5}\left(\lambda_{vx}x + \lambda_{vy}y + \lambda_{vz}z\right) \tag{4.13}$$

$$\dot{\lambda}_y = \frac{\lambda_{vy}\mu}{r^3} - \frac{3\mu y}{r^5}\left(\lambda_{vx}x + \lambda_{vy}y + \lambda_{vz}z\right) \tag{4.14}$$

$$\dot{\lambda}_z = \frac{\lambda_{vz}\mu}{r^3} - \frac{3\mu z}{r^5}\left(\lambda_{vx}x + \lambda_{vy}y + \lambda_{vz}z\right) \tag{4.15}$$

The state, ν, is no longer used, and the orientation of $\hat{\mathbf{L}}^*$ can be described using one angle, as stated in Section 3.3. Equations (4.13–4.14) no longer minimize the Hamiltonian and, therefore, no longer describe optimal motion, only an approximation of optimal motion. We explore the validity of the approximation in Section 6.5.2.

To non-dimensionalize the equations of motion, we set $\mu = 1$, $R_* = 1$ DU in Equation 3.2, and define a dimensionless thrust variable, T, as

$$T = \frac{BIL/m}{R_0 n^2} \tag{4.16}$$

where n is the dimensional mean motion at the equatorial radius of the attracting body, R_0. The dimensionless form of the solution puts distances in terms of distance units, DU, and velocity in terms DU/TU, allowing the solutions to be generalized for any attracting body and spacecraft mass. One circular orbit at 1 DU has a period of 2π TU.

Boundary Value Problem

To complete the problem formulation for the 3D Cartesian system, we establish a boundary value problem for a phasing maneuver with known initial conditions on the state and desired final conditions on the state. Specifically, the initial conditions are

$$x(0) = r_0 \qquad y(0) = 0 \qquad z(0) = 0 \qquad v_x(0) = 0 \qquad v_y(0) = \sqrt{\frac{1}{r_0}} \qquad v_z(0) = 0 \quad (4.17)$$

corresponding to a circular orbit in the equatorial plane. The desired final conditions are

$$x(t_f) = r_0 \cos(\phi + n_0 t_f) \qquad y(t_f) = r_0 \sin(\phi + n_0 t_f) \qquad z(t_f) = 0 \qquad (4.18)$$

$$v_x(t_f) = -\frac{\sin(\phi + n_0 t_f)}{\sqrt{r_0}} \qquad v_x(t_f) = \frac{\cos(\phi + n_0 t_f)}{\sqrt{r_0}} \qquad v_z(t_f) = 0$$

where $n_0 = \sqrt{1/r_0^3}$ is the dimensionless initial mean motion at the starting radius r_0. The final conditions match the position and velocity of the target spacecraft. One benefit of non-dimensionalizing the system is that the time of flight is proportional to the change in true anomaly.[11] We find a solution when the difference between the EDT state at $t = t_f$ and the boundary conditions approaches zero and when the end conditions of the costates satisfy the transversality conditions of Pontryagin's Minimum Principle. This difference is called the residual error.

The unknowns in this boundary value problem are the initial conditions for the costates and the final time. We can set λ_{x0} to an arbitrary positive real number, in this case $\lambda_{x0} = 1$, because the Hamiltonian is linear in the costates.[8,5] This choice ensures that the costates satisfy the first condition in Pontryagin's Minimum Principle.

4.1.2 Optimal 2D Equations of Motion in Cartesian Coordinates

We use Equations (3.8-3.10) to form the Hamiltonian for the 2D Cartesian system:

$$H = \lambda_x v_x + \lambda_y v_y + \lambda_{v_x}\left(-\frac{\mu}{r^3}x + \frac{BIL}{m}\cos\psi\right) + \lambda_{v_y}\left(-\frac{\mu}{r^3}y + \frac{BIL}{m}\sin\psi\right) \quad (4.19)$$

Solving the partial differential equation,

$$\frac{\partial H}{\partial \psi} = -\lambda_{v_x}\frac{BIL}{m}\sin\psi + \lambda_{v_y}\frac{BIL}{m}\cos\psi = 0 \quad (4.20)$$

yields the optimal control law:

$$\psi = \tan^{-1}\left(\frac{-\lambda_{vy}}{-\lambda_{vx}}\right) \quad (4.21)$$

Like the 3D Cartesian system, we require the negative signs in Equation (4.21) to satisfy the Legendre-Clebsch condition:

$$\frac{\partial^2 H}{\partial \psi^2} = -\lambda_{v_x}\frac{BIL}{m}\cos\psi - \lambda_{v_y}\frac{BIL}{m}\sin\psi \geq 0 \quad (4.22)$$

Putting Equation (4.21) into the following form,

$$\sin\psi = \frac{-\lambda_{vy}}{\sqrt{\lambda_{vy}^2 + \lambda_{vx}^2}} \quad (4.23)$$

$$\cos\psi = \frac{-\lambda_{vx}}{\sqrt{\lambda_{vy}^2 + \lambda_{vx}^2}} \quad (4.24)$$

and inserting Equations (4.23–4.24) in Equation 4.22, the second derivative of the

Hamiltonian is,

$$\frac{\partial^2 H}{\partial \psi^2} = \frac{BIL}{m}\sqrt{\lambda_{vx}^2 + \lambda_{vy}^2} \geq 0 \tag{4.25}$$

which satisfies the Legendre-Clebsch condition for minimization.

Substituting Equation (4.21) into Equations (3.9-3.10) gives the minimum-time equations of motion,

$$\dot{v}_x = -\frac{\mu}{r^3}x + \frac{BIL\cos\left(\tan^{-1}\left(\frac{-\lambda_{vy}}{-\lambda_{vx}}\right)\right)}{m} \tag{4.26}$$

$$\dot{v}_y = -\frac{\mu}{r^3}y + \frac{BIL\sin\left(\tan^{-1}\left(\frac{-\lambda_{vy}}{-\lambda_{vx}}\right)\right)}{m} \tag{4.27}$$

The differential equations for the costates give the remaining equations required to solve the system:

$$\dot{\lambda}_x = \frac{\lambda_{vx}\mu}{r^3} - \frac{3\mu x}{r^5}\left(\lambda_{vx}x + \lambda_{vy}y - R_* H_0 \cos\psi\right) \tag{4.28}$$

$$\dot{\lambda}_y = \frac{\lambda_{vy}\mu}{r^3} - \frac{3\mu y}{r^5}\left(\lambda_{vx}x + \lambda_{vy}y - R_* H_0 \sin\psi\right) \tag{4.29}$$

$$\dot{\lambda}_{vx} = -\lambda_x \tag{4.30}$$

$$\dot{\lambda}_{vy} = -\lambda_y \tag{4.31}$$

Finally, we use Equation (4.16) to get the optimal, non-dimensional acceleration and costate equations:

$$\dot{v}_x = -\frac{\mu}{r^3}x + TR_0 n^2 \cos\left(\tan^{-1}\left(\frac{-\lambda_{vy}}{-\lambda_{vx}}\right)\right) \tag{4.32}$$

$$\dot{v}_y = -\frac{\mu}{r^3}y + TR_0 n^2 \sin\left(\tan^{-1}\left(\frac{-\lambda_{vy}}{-\lambda_{vx}}\right)\right) \tag{4.33}$$

$$\dot{\lambda}_x = \frac{\lambda_{vx}\mu}{r^3} - \frac{3\mu x}{r^5}\left(\lambda_{vx}x + \lambda_{vy}y - \frac{H_0}{R_0 n^2}\cos\psi\right) \tag{4.34}$$

$$\dot{\lambda}_y = \frac{\lambda_{vy}\mu}{r^3} - \frac{3\mu y}{r^5}\left(\lambda_{vx}x + \lambda_{vy}y - \frac{H_0}{R_0 n^2}\sin\psi\right) \tag{4.35}$$

Ignoring the small partial derivatives of B yield the following dimensionless costate equations:

$$\dot{\lambda}_x = \frac{\lambda_{vx}\mu}{r^3} - \frac{3\mu x}{r^5}\left(\lambda_{vx}x + \lambda_{vy}y\right) \tag{4.36}$$

$$\dot{\lambda}_y = \frac{\lambda_{vy}\mu}{r^3} - \frac{3\mu y}{r^5}\left(\lambda_{vx}x + \lambda_{vy}y\right) \tag{4.37}$$

As stated in Section 4.1.1, neglecting terms in the costate differential equations, no matter how small, make the trajectory described by the equations of motion only an approximation of the optimal trajectory. We study the validity of the approximation in Section 6.5.1.

Boundary Value Problem

The boundary conditions for the 2D phasing maneuver are identical to those for the 3D phasing maneuver except that there is no z-component. The initial conditions are,

$$x(0) = r_0 \qquad y(0) = 0 \qquad v_x(0) = 0 \qquad v_y(0) = \sqrt{\frac{1}{r_0}} \tag{4.38}$$

and the end conditions are,

$$x(t_f) = r_0\cos\left(\phi + n_0 t_f\right) \qquad y(t_f) = r_0\sin\left(\phi + n_0 t_f\right)$$

$$v_x(t_f) = -\frac{\sin\left(\phi + n_0 t_f\right)}{\sqrt{r_0}} \qquad v_x(t_f) = \frac{\cos\left(\phi + n_0 t_f\right)}{\sqrt{r_0}}$$

Like the 3D Cartesian system, the unknowns in this boundary value problem are the initial conditions for the costates and the final time. Also, to scale our solutions and to ensure that the costates satisfy the first condition in Pontryagin's Minimum Principle, we set $\lambda_{x0} = 1$, an arbitrary positive real number. We find a solution when the residual approaches zero and when the end values of the costates satisfy the transversality conditions.

4.2 Optimal Control Law and Equations of Motion for Orbit Raising Maneuvers

We use the same procedure to optimize the polar equations of motion as we do to optimize the Cartesian equations of motion. First we start with Equations (3.11–3.13) to obtain the variational Hamiltonian,

$$H = \lambda_r u + \lambda_u \left(\frac{v^2}{r} - \frac{\mu}{r^2} + TR_0 n^2 \sin\bar{\psi} \right) + \lambda_v \left(-\frac{uv}{r} + TR_0 n^2 \cos\bar{\psi} \right) \tag{4.39}$$

and solve for an optimal control law that maximizes the Hamiltonian.

$$\frac{\partial H}{\partial \bar{\psi}} = \lambda_u TR_0 n^2 \cos\bar{\psi} - \lambda_v TR_0 n^2 \sin\bar{\psi} = 0 \tag{4.40}$$

$$\bar{\psi} = \tan^{-1}\left(\frac{\lambda_u}{\lambda_v}\right) \tag{4.41}$$

Unlike the Cartesian systems, we do not require negative signs in front of the costates because we wish to satisfy the Legendre-Clebsch condition for maximization:

$$\frac{\partial^2 H}{\partial \bar{\psi}^2} = -\lambda_u T R_0 n^2 \sin\bar{\psi} - \lambda_v T R_0 n^2 \cos\bar{\psi} \leq 0 \tag{4.42}$$

After splitting the control law into sin and cos,

$$\sin\bar{\psi} = \frac{\lambda_u}{\sqrt{\lambda_u^2 + \lambda_v^2}} \tag{4.43}$$

$$\cos\bar{\psi} = \frac{\lambda_v}{\sqrt{\lambda_u^2 + \lambda_v^2}} \tag{4.44}$$

the second derivative of the Hamiltonian is,

$$\frac{\partial^2 H}{\partial \bar{\psi}^2} = -T R_0 n^2 \sqrt{\lambda_u^2 + \lambda_v^2} \leq 0 \tag{4.45}$$

Maximizing the Hamiltonian and applying the end boundary conditions move the EDT to the desired circular orbit in minimum time.[8]

Substituting Equation (4.41) into Equations (3.11–3.13) yields the optimal, non-dimensional polar equations of motion for the states:

$$\dot{r} = u \tag{4.46}$$

$$\dot{u} = \frac{v^2}{r} - \frac{\mu}{r^2} + T R_0 n^2 \sin\left(\tan^{-1}\left(\frac{\lambda_u}{\lambda_v}\right)\right) \tag{4.47}$$

$$\dot{v} = -\frac{uv}{r} + T R_0 n^2 \cos\left(\tan^{-1}\left(\frac{\lambda_u}{\lambda_v}\right)\right) \tag{4.48}$$

The optimal, non-dimensional polar equations of motion for the costates are:

$$\dot{\lambda}_r = -\frac{\partial H}{\partial r} = -\lambda_u \left(-\frac{v^2}{r^2} + 2\frac{1}{r^3} - R_0 n^2 \frac{\partial T}{\partial r} \sin\bar{\psi} \right) - \lambda_v \left(\frac{uv}{r^2} - R_0 n^2 \frac{\partial T}{\partial r} \cos\bar{\psi} \right) \tag{4.49}$$

$$\dot{\lambda}_u = -\frac{\partial H}{\partial u} = -\lambda_r + \lambda_v \frac{v}{r} \tag{4.50}$$

$$\dot{\lambda}_v = \frac{\partial H}{\partial v} = -2\lambda_u \frac{v}{r} + \lambda_v \frac{u}{r} \tag{4.51}$$

where

$$\frac{\partial T}{\partial r} = \frac{-3H_0 iL}{mR_0 n^2 r^4} \tag{4.52}$$

If we ignore the terms containing partial derivatives of T, as we did in previous sections, we obtain the following equation for $\dot{\lambda}_r$:

$$\dot{\lambda}_r = -\lambda_u \left(-\frac{v^2}{r^2} + 2\frac{1}{r^3} \right) - \lambda_v \frac{uv}{r^2} \tag{4.53}$$

Using Equation (4.53) no longer makes the trajectory described by it optimal. The resulting trajectory is only an approximation of optimality.

4.2.1 Boundary Value Problem

The initial boundary conditions for the orbit-raising maneuver are,

$$r(0) = r_1 \qquad u(0) = 0 \qquad v(0) = \frac{1}{\sqrt{r_1}} \tag{4.54}$$

corresponding to a circular orbit at radius, r_1. The end conditions are,

$$r(t_f) = r_2 \qquad u(0) = 0 \qquad v(0) = \frac{1}{\sqrt{r_2}} \tag{4.55}$$

which correspond to another circular orbit at radius, r_2.

Like the Cartesian systems, the unknowns in this boundary value problem are the initial conditions for the costates and the final time, and we set $\lambda_{r_0} = 1$, an arbitrary positive number, to satisfy Pontryagin's Minimum Principle's first condition. We find a solution when costates at time $t = t_f$ satisfy the transversality conditions and when the EDT's state represents that of a circular orbit at the target radius.

4.3 Summary

Using Pontryagin's Minimum Principle, we derive the optimal, non-dimensional equations of motion for the 2D and 3D Cartesian systems and the polar system. We also present the boundary conditions and the unknowns that need to be solved for all three maneuvers. The next chapter contains the solutions to these boundary value problems and the analysis of those solutions.

Chapter 5

Solution Algorithm

Finding a suitable solution algorithm took years of research as well as trial and error. Our solution algorithm is similar to the one stated in Ref. 1. We start by using Adaptive Simulated Annealing to narrow down the search space. Next, we use Newton's method to bring the error in the solution to within a specified tolerance, and lastly, we use numerical continuation to find a set of solutions for varying values of the parameters.

5.1 Adaptive Simulated Annealing

As stated in Chapter 2, ASA is a global, stochastic optimization method that uses the system's cost function and probability to find the optimal solution. ASA can be applied to constrained or unconstrained finite-dimensional problems. A diagram of the algorithm is shown in Figure 5.1. ASA begins by choosing random values for the time of flight and initial Lagrange costates, stated as the vector $\xi_{i=i_0}$ in the algorithm, within the search space and uses an assigned initial temperature, ϑ_0, to find the next the best candidate point, ξ_{i+1}. The algorithm uses the system's performance index, in

this case the residual, to evaluate the energy value for ξ_{i+1}, $E(\xi_{i+1})$. If the new energy value is lower than old best energy value, i.e. $\Delta E = E(\xi_i) - E(\xi_{i+1})$ is negative, then ξ_{i+1} is accepted. If not, then the probability of ξ_{i+1} being accepted is proportional to $\exp(\Delta E/\vartheta_i)$. After a certain number of points are accepted, the temperature lowers to ϑ_{i+1}. The algorithm is adaptive because as the temperature decreases, ASA searches the contours of the search space with finer resolution.[1]

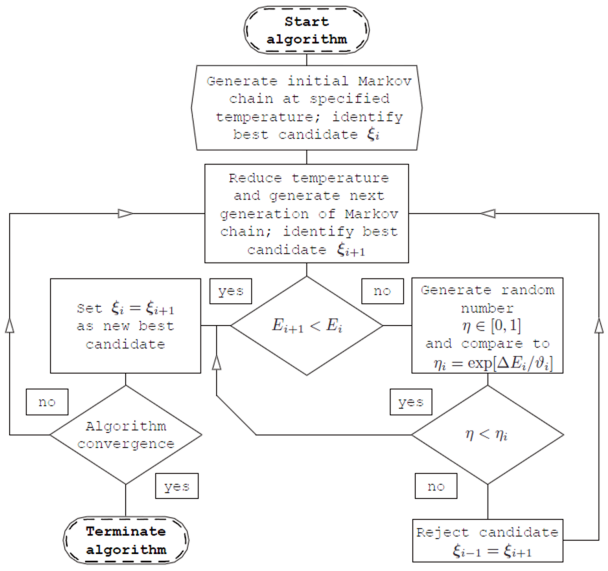

Figure 5.1: Adaptive Simulated Annealing Algorithm[1]

We can change many parameters in the ASA algorithm to change its performance. The most important parameter is the reduction rate for the temperature. If the rate is too high, then ASA converges to a non-optimal solution, and if the rate is too low, then ASA becomes computationally expensive. The rate we use is $\vartheta_{i+1} = 0.96\vartheta_i$. Another parameter we change determines how ASA picks a new point. The step size from one point to the next is determined by the acceptance rate of ξ_i. If the acceptance rate is higher than 60%, then the step size increases, and if it is lower than 40%, then the step size decreases. Other parameters we can change are the number of iterations required to lower the temperature and the number of iterations

required to measure the acceptance rate.

5.2 Newton's Method

Once ASA converges to a small area containing the solution, we use Newton's method to reduce the error below a certain tolerance. Newton's method is a common way to solve nonlinear root finding problems. It has a quadratic rate of convergence, but has a small radius of convergence, so the initial guess from ASA must be close to the solution. From our experience, the error in the initial guess must be within 5-10% for Newton's Method to converge.

The iterative equation for Newton's Method is

$$\mathbf{x}_{i+1} = x_i - \left(\frac{\partial \mathbf{f}}{\partial \mathbf{x}}\right)^{-1} \mathbf{f} \tag{5.1}$$

We use the finite difference method with a step size of $\epsilon^{2/3}$ to evaluate the Jacobian, where ϵ is the smallest number a computer processor can handle such that $1 + \epsilon > \epsilon$. Newton's method iterates until the norm of the residual goes below 10^{-10}.

5.3 Numerical Continuation

Having found one solution, we find additional solutions using numeric continuation.[1] Continuation, in its most basic form, is when a previous solution, $\mathbf{x}^*$, to a problem with parameter, p^*, is used to make an initial guess for a solution with a new parameter, $p^* + \Delta p$. In our approach, we take an Euler step from the previous solution to form the initial guess for the new solution:

$$\Delta \mathbf{x} = \left[\frac{\partial \mathbf{f}(\mathbf{x}, p)}{\partial \mathbf{x}}\right]^{-1} \Bigg|_{\mathbf{x}^*, p^*} \frac{\partial \mathbf{f}(\mathbf{x}, p)}{\partial p} \Delta p \tag{5.2}$$

where the Jacobian is evaluated at the previous solution. We then use Newton's method to obtain the next solution. We vary two parameters in our analysis, the initial thrust, T_0, and the phase angle, ϕ. Finding solutions for a wide range of T_0 and ϕ gives the solution space for a particular maneuver.

5.4 Finding Solutions for all Three Maneuvers

We use ASA to find the first optimal solution for a 2D phasing maneuver, but not for the other two maneuvers. The solutions for 2D case serve as initial guesses for the initial costates and time of flight for the 3D case. We find the initial conditions for the orbit-raising maneuver by using the approximate methods given in Ref. 8.

5.5 Summary

Our solution algorithm has three parts. First, Adaptive Simulated Annealing narrows down search space to a small region containing the solution using a global, stochastic approach. Next, we use Newton's method to reduce the residual to below 10^{-10}. Lastly, we use numerical continuation to obtain the solution space for optimal control problem. In the next chapter, we present our results.

Chapter 6

Results and Solutions

In this chapter, we present numerical solutions for phasing maneuvers with a non-tilted magnetic dipole, orbit-raising maneuvers, and phasing maneuvers with a tilted magnetic dipole using the costate differential equation approximations stated in Chapter 4. We begin by giving sample solutions for all three maneuvers. After that, we compare the EDT solutions with solutions in the literature and look at the solution space as a whole and describe the patterns lying within it. Lastly, we test the validity of making the costate differential equation approximation.

6.1 Sample Numerical Solutions

The following sample solutions give the basic structure of the optimal solutions for all three maneuvers. For all solutions, 1 DU is the radius of the attracting body.

6.1.1 2D Phasing Maneuvers

Figure 6.1 shows a sample trajectory and control solution with an exaggerated thrust and phase angle and an initial radius $r_0 = 1.062716$. In the figure, the small circle is

the starting position of the EDT, the "×" is the starting position of the target, the dotted line is the target circular orbit, and the solid line is the trajectory. The EDT begins by thrusting inward to lower the altitude. Lowering the altitude allows the EDT to travel faster than its target. As the altitude decreases, the thrust increases because the strength of the magnetic field increases. After lowering the altitude, the EDT rotates the thrust toward the velocity direction. Near the middle of the maneuver, the EDT rotates away from the velocity direction to slow down and rendezvous with target in the original circular orbit. The example maneuver uses a large current with an initial thrust, $T_0 = 0.76370$, and a large phase angle, $\phi = 1.49$ rad, so that we may easily show the trajectory. For thrusts at a more reasonable level ($T_0 < 0.1$), a low-thrust trajectory is difficult to distinguish from the target orbit.

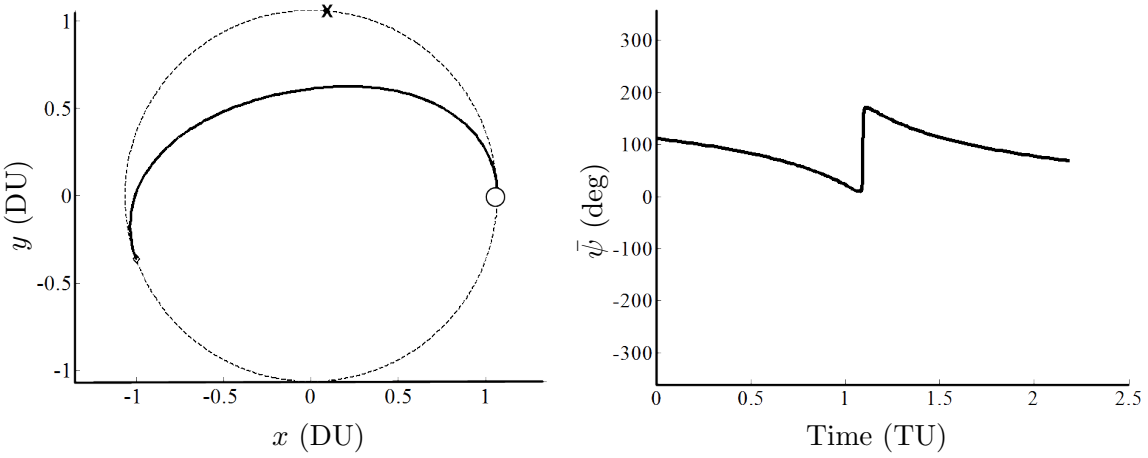

Figure 6.1: 2D Phasing Maneuver Trajectory Example ($T_0 = 0.76370$, $\phi = 1.49$)

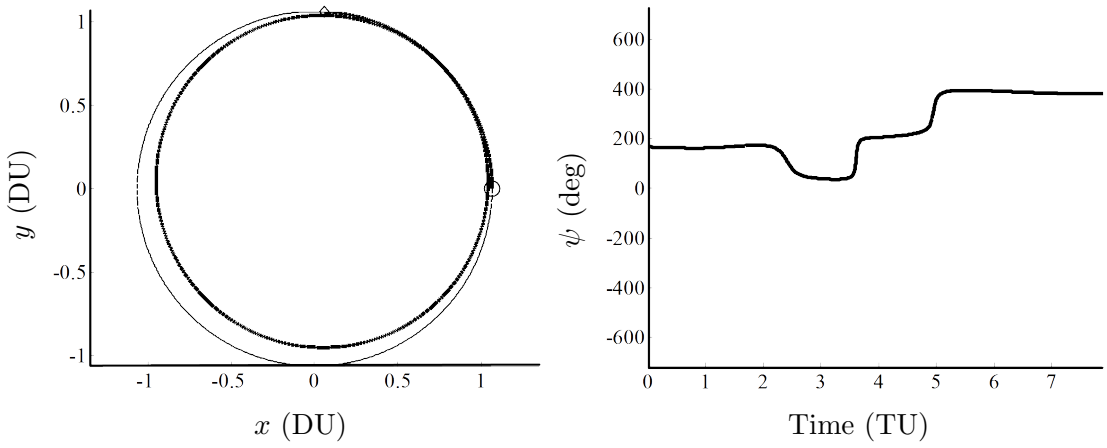

Figure 6.2: 3D Phasing Maneuver Trajectory Example ($T_0 = 0.01531$, $\phi = 0.60$ rad)

6.1.2 3D Phasing Maneuvers

Figure 6.2, 6.3, and 6.4 show a sample trajectory and control solution for a realistic thrust ($T_0 = 0.01531$) and phase angle ($\phi = 0.60$ rad). The optimal control plot in Figure 6.2 shows ψ, as illustrated by Figure 3.2, but the figure is not an intuitive way to view the control history. We use Figures 6.3 and 6.4 to better illustrate the control. Figure 6.3 gives the inertial position vector components for the EDT, and Figure 6.4 gives the thrust vector component in the velocity direction, T_v, the component in the nadir direction, T_n, and the component in the $\hat{\mathbf{n}}_\mathbf{3}$ direction, T_z. The EDT begins a 3D phasing maneuver by thrusting inward and then by thrusting in the velocity direction. The control history plot shows a series of sudden rotations instead of just one rotation. For maneuvers that last less than half an orbit, there are two sudden rotations. And for maneuvers lasting longer than half an orbit, there are three sudden rotations. When there are two sudden rotations, they occur before and after and the same distance away from the midpoint in the maneuver. When there are three sudden

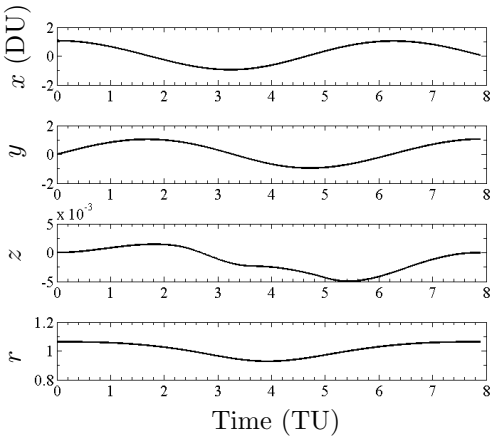

Figure 6.3: Inertial Position Vector Components and Orbit Radius

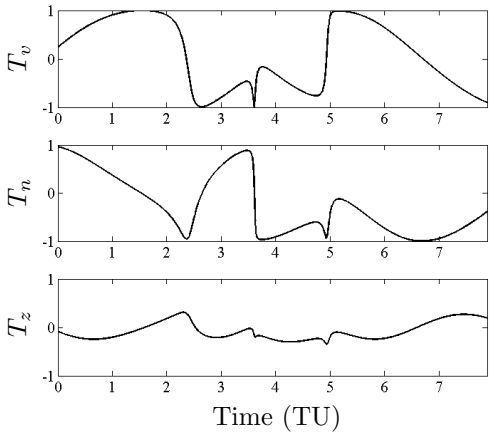

Figure 6.4: Normalized Thrust Vector Components

rotations, the middle rotation occurs at the mid-point, and the other two are equally spaced on either side. The EDT finishes its maneuver by thrusting outward to meet its target.

6.1.3 Orbit Raising Maneuvers

There are two kinds of orbit-raising trajectories that categorize the whole solution space: multi-revolution maneuvers and short duration maneuvers. Figure 6.5 shows an example of an orbit-raising trajectory and optimal control history for a multi-revolution maneuver. The inner dotted line is the starting radius, $r_1 = 1.062716$ DU, the outer dotted line is the final radius, $r_2 = 1.378$ DU, and the solid line is the EDT trajectory. The EDT always thrusts near the velocity direction to add energy to the orbit, and the thrust direction oscillates with a period close to the orbit period. The oscillation is not a steady sinusoidal wave. The intervals where $\bar{\psi}$ increases have a smaller slope than when $\bar{\psi}$ decreases. The steeper drop in $\bar{\psi}$ occurs near $\theta = \pi/2$. Also, as the radius increases, the thrust magnitude decreases because the magnetic field gets weaker.

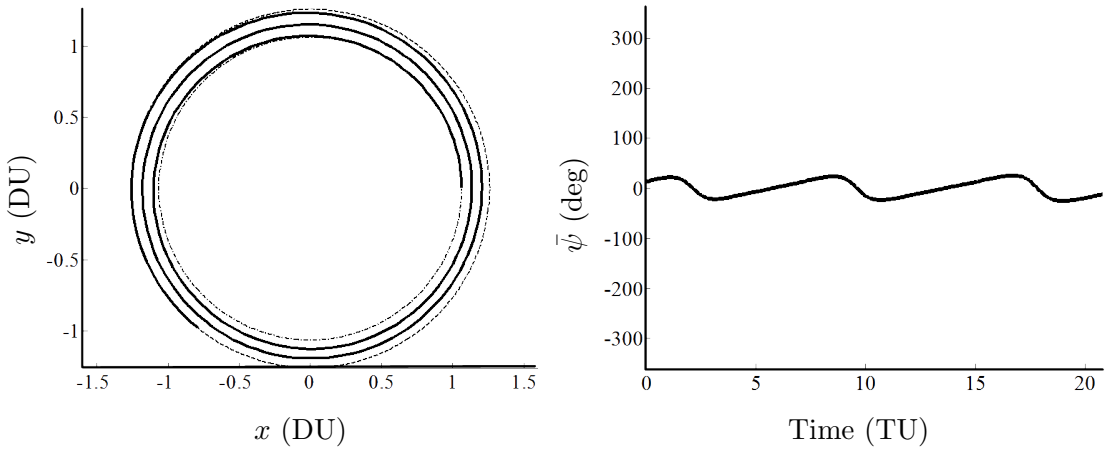

Figure 6.5: Multi-Revolution Orbit Raising Trajectory Example (T_0 = 0.005108, r_2 = 1.258 DU)

Figure 6.6 shows an example of a short duration maneuver. The flight time for orbit-raising maneuvers decreases as r_2 decreases and T increases. If T is high enough ($T_0 \approx 0.1$), the thrust becomes more influential in comparison to the gravity force, and the EDT aims straight for its target, like in a phasing maneuver. This is why the control history looks similar to that of a phasing maneuver. The EDT begins by thrusting outward and ends by thrusting inward. Unlike a phasing maneuver, the change in direction does not occur midway through the maneuver. The time when the thrust changes direction varies depending on the input parameters.

A common trait for all orbit-raising maneuvers is that as the orbit radius increases, the thrust decreases because the magnetic field weakens. Figure 6.7 plots for the orbit radius and thrust.

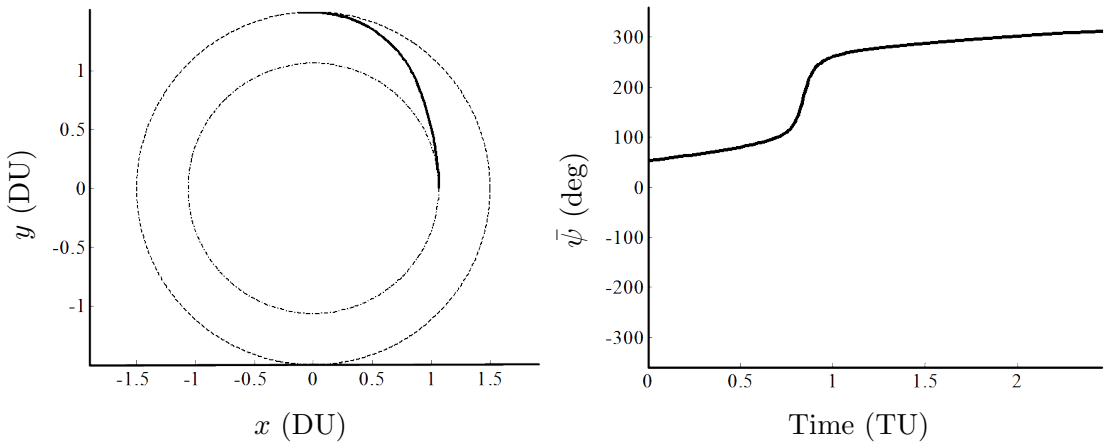

Figure 6.6: Short Duration Orbit Raising Trajectory Example ($T_0 = 0.4725$, $r_2 = 1.498$ DU)

6.2 Comparing Optimal EDT and Constant-Thrust Maneuvers

We can better gauge the performance of the EDT by comparing the EDT solutions to solutions established in the literature for constant-thrust spacecraft.

6.2.1 2D Phasing Maneuvers

We compare the results to the work presented in Ref. 11, which focused on constant-thrust, minimum-time phasing maneuvers in two-dimensional space. The authors provided several solutions that were representative of their work and revealed patterns in their solutions. We compare two aspects of their work to the two-dimensional EDT optimal control problem. One comparison is the trajectory. The other is the near-invariance of the initial costates when changing T_0 and ϕ by the same order of magnitude.

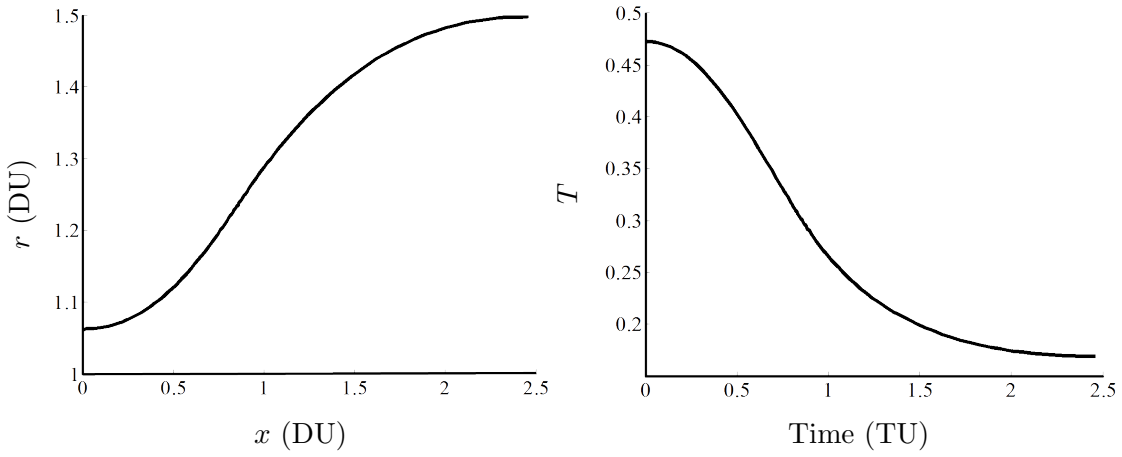

Figure 6.7: Comparison Between Orbit Radius and Thrust ($T_0 = 0.4725$, $r_2 = 1.498$ DU)

Trajectory Comparison

When comparing the optimal trajectory of a constant current EDT with that of a constant thrust spacecraft, intuition suggests that the EDT will catch up to its target faster because thrust increases when the orbit radius decreases, in accordance with the definition of a Lorentz force. Calculations show that the EDT does indeed arrive at its target more quickly than a constant-thrust spacecraft. When comparing the flight times presented in Ref. 11 with the EDT flight times, the EDT reaches its target faster, as shown in Table 6.1. The difference in the flight time is more pronounced in large phase angle maneuvers. For the case with $\phi = 0.54$, the difference in the time of flight is 0.0882 TU while the difference in the time of flight is only 0.001525 TU for $\phi = 0.0074$ rad. A small phase angle maneuver does not allow the EDT to dip far enough inside the target orbit to use its advantage over the constant-thrust spacecraft.

One similarity between the EDT and the constant-thrust spacecraft is the pattern

Table 6.1: Lagrange Costate and Time of Flight Comparison

T_0		0.5	0.5	0.05	0.005	0.005	0.005
ϕ		1.46	0.54	0.89	0.0074	0.022	0.1
EDT	λ_{y_0}	0.42896	0.099345	0.34992	0.18569	0.43658	0.33357
	$\lambda_{v_{x0}}$	0.62643	0.65774	0.44331	0.72805	0.69926	0.43892
	$\lambda_{v_{y0}}$	0.42613	-0.039660	0.98215	0.000697	0.49590	0.99619
	t_f	2.51007	1.95232	5.42443	2.45092	3.78494	6.16831
Constant Thrust	λ_{y_0}	0.47313	0.14480	0.34156	0.18627	0.43713	0.33270
	$\lambda_{v_{x0}}$	0.63251	0.66574	0.43092	0.72812	0.69905	0.43752
	$\lambda_{v_{y0}}$	0.49960	0.00012	1.00027	0.001362	0.49755	0.99824
	t_f	2.78398	2.04048	5.58198	2.45245	3.79228	6.18639

of their control angle time histories. Both spacecraft follow the same pattern as the example solution described above. There are also cases for both spacecraft where the rotation in the middle of the maneuver is clockwise when looking down on the orbit plane and cases where the rotation is counter-clockwise, depending on the input parameters. The magnitude of the rotations is similar for both spin directions, and these changes in rotation form bifurcation lines in the $T_0 - \phi$ parameter plane. We present a more detailed analysis of how varying the input parameters affects the control angle in Section 6.3.1.

Near-Invariance of the Initial Lagrange Costates

One conclusion in Ref. 11 is that when T_0 and ϕ are both increased by an order of magnitude, the values of the initial Lagrange costates and the time of flight change by a small amount for moderate and low thrust cases. The near-invariance of the initial costates is important because it allows us to find a wide range of solutions once we find one solution. The EDT two-dimensional optimal control problem also has this trait.

Table 6.2 gives three representative examples that illustrate the near-invariance for moderate and low thrust cases and shows the claim's limitations. The first example,

the case with the lowest thrust value, has the least amount of variance when T_0 and ϕ increase by an order of magnitude. The costates and the time of flight are constant to three decimal places. The second example shows an invariance between the two costate sets to two significant digits. The last example compares a high-thrust, high phase angle case ($T_0 = 0.5$, $\phi = 1.46$) with a thrust and phase angle one order of magnitude smaller. This comparison shows the largest change of all three cases, much more so than the constant-thrust case with similar parameters. Further exploration shows that there is always a large variation in the initial costates when large values of T_0 and ϕ decrease by an order of magnitude. The varying thrust magnitudes experienced during the EDT phasing maneuver cause larger variations in the initial costates than in the constant-thrust problem. The varying thrust plays a role in varying the initial costates with smaller combinations of T_0 and ϕ as well, but has less of an effect because the altitude does not decrease significantly during the maneuver. The initial costates for the constant-thrust cases are closer to constant values, by one or more significant figures, for all explored combinations of T_0 and ϕ.

Table 6.2: Near-Invariance of the Initial Costates for 2D Phasing Maneuvers

	T_0	ϕ	λ_{y_0}	$\lambda_{v_{x0}}$	$\lambda_{v_{y0}}$	t_f
1	0.0005	0.00074	0.18527	0.72864	-0.0003115	2.45355
	0.005	0.0074	0.18569	0.72805	0.000697	2.45092
2	0.009197	0.001	-2.52311	0.34754	-0.85886	0.66334
	0.09197	0.01	-2.48727	0.34688	-0.84637	0.66314
3	0.05	0.146	0.38861	0.71940	0.32728	3.18374
	0.5	1.46	0.42896	0.62643	0.42613	2.51007

6.2.2 3D Phasing Maneuvers

In this section, we compare the trajectories for 3D EDT phasing maneuvers in the equatorial plane, 2D EDT phasing maneuvers, and the phasing maneuvers in Ref. 11.

We also investigate any invariance properties in the solutions for 3D EDT phasing maneuvers.

Trajectory Comparison

Table 6.3 shows a list of initial costates and flight times for 3D EDT phasing maneuvers, 2D EDT phasing maneuvers, and constant-thrust phasing maneuvers for a wide range of initial thrusts and phase angles. In all cases, the EDT performs a phasing maneuver faster, as expected, when the magnetic dipole is not tilted than when it is tilted. In general, an EDT in a tilted magnetic field must thrust out of the orbit plane and cannot use all of its thrust to pursue its target. The difference between the tilted and non-tilted flight times increases when thrust increases.

Table 6.3: Lagrange Costate and Time of Flight Comparison

T_0		0.002556	0.2556	0.2556	0.01278	0.04089
ϕ		0.01	0.10	1.49	1.00	0.58
3D EDT	λ_{y_0}	0.40860	-0.45630	0.44960	-0.0023637	0.37585
	λ_{z_0}	-0.39038	0.35224	-0.63426	-0.12558	-0.23455
	$\lambda_{v_{x0}}$	0.75581	0.88464	0.63291	0.059067	0.53744
	$\lambda_{v_{y0}}$	0.52854	-0.38981	0.76093	1.15315	1.01212
	$\lambda_{v_{z0}}$	-0.74076	-1.35833	-0.84383	0.32019	-0.59554
	t_f	3.91837	1.77893	3.69370	9.87708	5.70802
2D EDT	λ_{y_0}	0.41968	-0.81178	0.46441	0.049094	0.40326
	$\lambda_{v_{x0}}$	0.78311	0.59135	0.66087	0.11900	0.57388
	$\lambda_{v_{y0}}$	0.46008	-0.59412	0.69054	1.20732	0.97074
	t_f	3.89499	1.30500	3.44979	9.79009	5.47890
Constant Thrust	λ_{y_0}	0.41993	-0.74152	0.48300	0.067334	0.39382
	$\lambda_{v_{x0}}$	0.78302	0.60546	0.65487	0.14400	0.55485
	$\lambda_{v_{y0}}$	0.46082	-0.57058	0.77365	1.11507	1.00606
	t_f	3.89758	1.35364	3.84697	10.43696	5.71180

In some cases, a constant-thrust spacecraft performs a phasing maneuver faster than an EDT performing a phasing maneuver in a tilted magnetic field. When the phase angle is small, the EDT cannot exploit its advantage of having variable thrust

because it does not dip deep below the target orbit. The inefficiencies of having to thrust out-of-plane overcome the thrust advantages, as evident in the first two cases in Table 6.3. However, when the phase angle is large, the EDT lowers its orbit radius more and can greatly increase its thrust and perform the maneuver faster than a constant-thrust spacecraft, as evident in the last three cases in Table 6.3, with the EDT only being slightly faster than the constant-thrust spacecraft in the last case.

A large difference between the 3D phasing maneuvers and the other two phasing maneuvers is that the control history for the 3D phasing maneuver has multiple sudden rotations. Each of the sudden rotations for the 3D phasing maneuver is roughly the same magnitude as the 2D rotations, so the EDT could complete several full rotations during a maneuver. However, the main sequence of events—thrusting inward, spinning, and thrust thrusting outward—is common between all three phasing maneuvers.

Near-Invariance of the Initial Lagrange Costates

The invariance properties of the 3D phasing maneuver solutions are not as strong as those for the 2D solutions. Table 6.4 shows three cases that illustrate the near-invariance of the initial costates and flight times for 3D phasing maneuvers. Like the 2D cases, the invariance properties do not hold for large thrusts or phase angles. In Case 1, $\phi \approx 4T_0$. Invariance to two decimal places of a pair of solutions does not occur until $T_0 = 2.556 \times 10^{-5}$ and $\phi = 0.0001$ increase to $T_0 = 2.556 \times 10^{-4}$ and $\phi = 0.001$. The 2D EDT phasing maneuver has two-decimal point invariance for solution pairs one order of magnitude higher. In Case 2, where $5\phi \approx T_0$, the costates are invariant, at most, to only one decimal point, but the time of flight is invariant to three decimal points. In Case 3, where $\phi \approx 39T_0$, the costates are invariant to three decimal points, at most, but the time of flight is only invariant to one decimal point.

Table 6.4: Near-Invariance of the Initial Costates for 3D Phasing Maneuvers

	T_0	ϕ	λ_{y_0}	λ_{z_0}	$\lambda_{v_{x0}}$	$\lambda_{v_{y0}}$	$\lambda_{v_{z0}}$	t_f
1	0.00002556	0.0001	0.40852	-0.38667	0.75628	0.52879	-0.73752	3.92720
	0.0002556	0.001	0.40834	-0.38495	0.75633	0.52807	-0.73525	3.92372
	0.002556	0.01	0.40860	-0.39038	0.75581	0.52854	-0.74076	3.91837
	0.02556	0.1	0.41119	-0.44481	0.75055	0.53309	-0.79499	3.86544
	0.2556	1.0	-0.45630	0.35224	0.88464	-0.38981	-1.35833	1.77893
2	0.002556	0.0005	-2.46716	-1.25045	1.95047	-1.89921	-7.57926	1.40599
	0.02556	0.005	-2.42357	-1.20616	1.91586	-1.86082	-7.40994	1.40621
	0.2556	0.05	-2.03633	-0.81187	1.61995	-1.52812	-5.95533	1.40937
3	0.00001278	0.00005	0.22654	-0.067180	0.33905	1.18373	-0.50611	8.34075
	0.0001278	0.005	0.22654	-0.067273	0.33902	1.18371	-0.50601	8.33874
	0.001278	0.05	0.22672	-0.068401	0.33903	1.18329	-0.50487	8.30437
	0.01278	0.5	0.22852	-0.078944	0.33906	1.17945	-0.49294	7.96363

When investigating other cases we find that when the thrust is greater than the phase angle, the time of flight is more invariant than the initial Lagrange costates, in general. The EDT has a high enough thrust, relative to the phase angle, to counter the time delays due to the out-of-plane motion. Conversely, when the thrust is less than the phase angle, the costates are more invariant than the time of flight. When T_0 and ϕ are roughly the same order of magnitude, neither have invariance to two decimal points unless $T_0 \approx \phi < 10^{-4}$. The invariance limit for 3D EDT phasing maneuvers is approximately one order of magnitude less than the invariance limit for 2D EDT phasing maneuvers.

6.2.3 2D Orbit Raising Maneuvers

Intuition suggests that a constant-thrust spacecraft can complete an orbit-raising maneuver faster than a constant-current EDT with the same initial thrust because thrust decreases as orbit radius increases. Table 6.5 confirms our intuition. In all cases, the constant-thrust spacecraft arrives at its target circular orbit sooner than the EDT; the difference in the flight times increases as r_2 increases. The last two

columns of Table 6.5 show the initial costates and flight times for two orbit-raising maneuvers with the same initial thrust but different target orbit radii. The difference in t_f with an initial thrust $T_0 = 0.01277$ is 4.451 for $r_2 = 1.380$ DU and 5.485 TU for $r_2 = 1.450$ DU.

Table 6.5: Costate and Flight Time Comparison for 2D Orbit Raising Maneuvers

T_0		0.01788	0.2299	0.1149	0.01277	0.01277
r_2		1.100	1.100	1.250	1.380	1.450
EDT	λ_{u_0}	0.64125	0.36600	0.65729	0.28498	0.16707
	λ_{v_0}	0.85177	0.12658	0.72516	1.25654	1.05085
	t_f	2.72973	0.81870	2.71062	14.89376	18.07511
Constant Thrust	λ_{u_0}	0.64029	0.36815	0.65516	0.23882	0.39335
	λ_{v_0}	0.85748	0.12876	0.75313	0.72154	1.05263
	t_f	2.66633	0.79788	2.40682	10.44294	12.58974

One similarity between the constant-thrust spacecraft and the EDT is that the initial costates are nearly equal for smaller increases in orbit radius. The maneuvers with $r_2 = 1.100$ DU have initial costates equal to two decimal places. A significant difference in the initial costates occurs when $r_2 > 1.2$ DU, as seen in the middle column of Table 6.5. Another similarity is that the shape of the control history plot for the constant-thrust spacecraft is the same as the EDT control histories described in Section 6.1.3.

Unlike phasing maneuvers, orbit-raising maneuvers do not have any invariance properties.

6.3 Solution Space Traits

In this section, we present the solution spaces for all three maneuvers. We vary the input parameters over a wide range and explain the patterns in the solutions.

6.3.1 2D Phasing Maneuvers

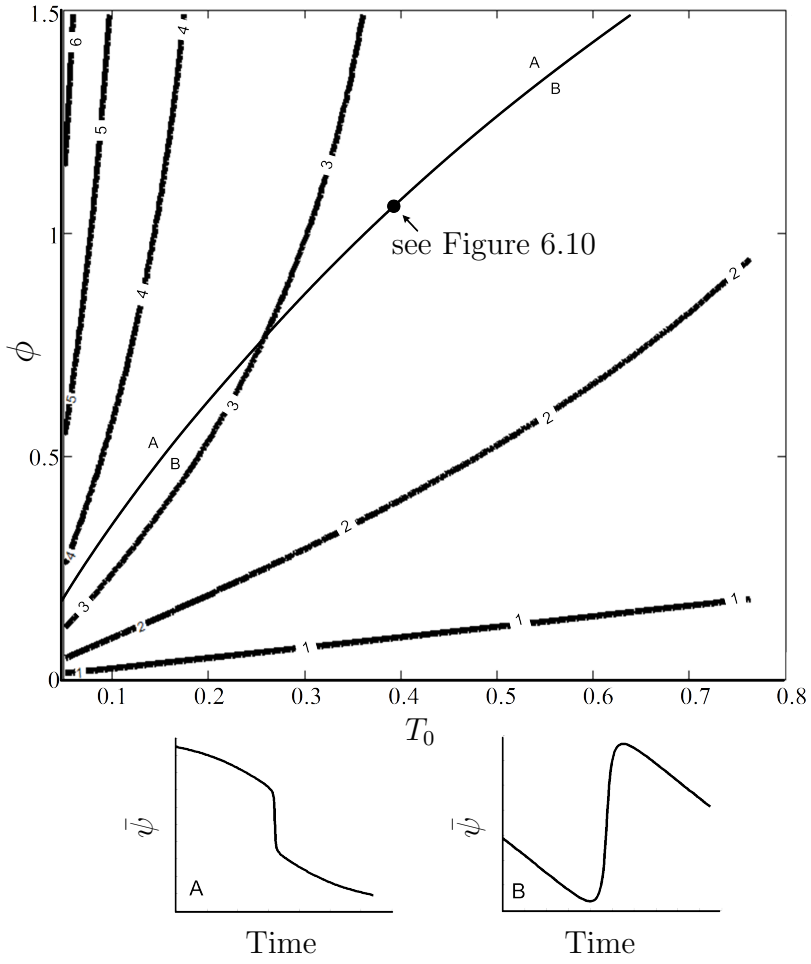

Figure 6.8: Control Angle Behavior and t_f Contour Plot for 2D Phasing Maneuvers

The solutions we obtained during this study can be summarized in two plots, Figures 6.8 and 6.9. Figure 6.8, the "high-end" plot, contains solutions for $0.05 < T_0 < 0.77$, and Figure 6.9, the "low-end" plot, contains solutions for $0.0013 < T_0 < 0.05$. The thick lines are lines of constant time of flight in TUs while the thin lines separate different types of control angle time histories. In both plots, flight time decreases, as intuition suggests, when the current increases and the phase angle decreases. However, the benefit of increasing the thrust to reduce the flight time diminishes as thrust increases, or in mathematical terms, $\partial^2 t_f/\partial\phi^2 < 0$. Small changes in phase angle

have a smaller effect on flight time when the phase angle is large than when the angle is small.

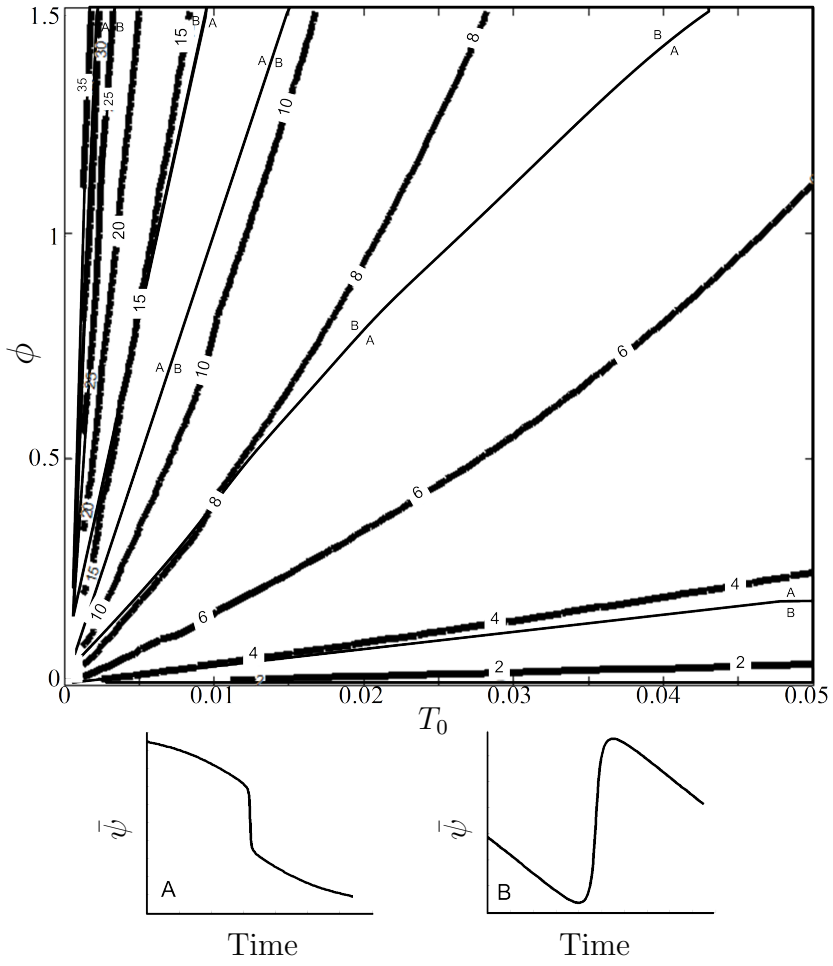

Figure 6.9: Control Angle Behavior and t_f Contour Plot for 2D Phasing Maneuvers

We can divide the control angle time history into two categories: one where $\bar{\psi}$ decreases suddenly in the middle (Group A) and one where $\bar{\psi}$ increases suddenly in the middle of the maneuver (Group B). A bifurcation line separates the two groups. Other than the spin direction, there is little difference in the control for a trajectory with parameters just above the bifurcation line and one with parameters just below it, as Figure 6.10 shows. The control histories for the second half of each maneuver is separated from each other by 360°.

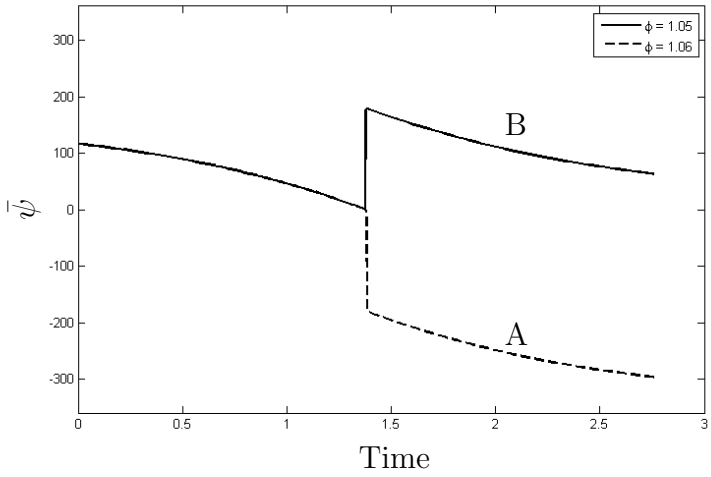

Figure 6.10: Illustrating the A-B Transition of Figures 6.8 and 6.9 ($T_0 = 0.3831$)

Many more bifurcation lines are present at the low end of the thrust scale. The bifurcation line from Figure 6.8 continues into the bottom portion of Figure 6.9, but several other bifurcation lines fan out like radial lines from the origin. The sectors between the lines alternate between Groups A and B, and the sectors become thinner as thrust decreases. The smallest initial thrust we solve for is $T_0 = 0.0013$. If we hold T_0 constant at this value and increase ϕ, we cross through several bifurcation lines. Figure 6.11 shows what happens to the control history as ϕ increases. The vertical axes are $\bar{\psi}$ and range from -360° to 360° for every plot. The horizontal axes are time, and the range on each plot is the time of flight for each maneuver. The flight time increases as ϕ increases. In the figure, the control alternates between rotating clockwise in the middle of the maneuver and rotating counter-clockwise.

Another feature in the control history becomes apparent as the time of flight increases. There is a small-amplitude oscillation in the control with a period equal to the target orbit period. This oscillation is present for all parameter values, but it only becomes visibly noticeable on a plot when the time of flight takes longer than one orbit. Also, the amplitude of the oscillation decreases as the input parameters approach the bifurcation line and reaches a maximum in the center of each sector.

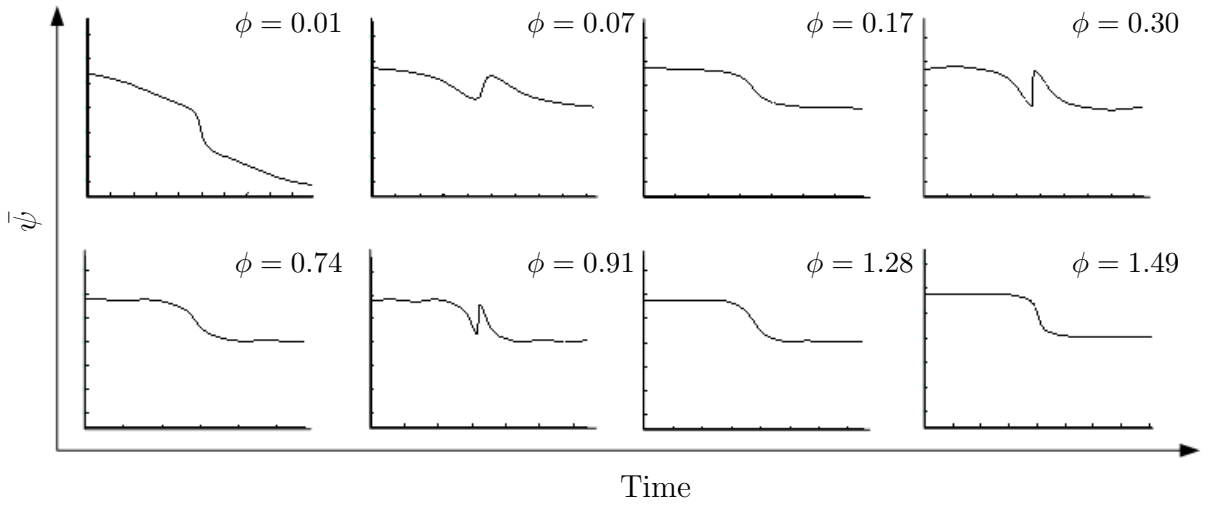

Figure 6.11: Control Angle vs. Time with $T_0 = 0.001278$ and Increasing ϕ

The numerical solutions show that the control solution space, while qualitatively uniform, is filled with a complex pattern of bifurcations and varying oscillations.

6.3.2 3D Phasing Maneuvers

We show the solution space contour plot for equatorial phasing maneuvers in a tilted magnetic field in Figure 6.12. It has a thrust range of $0.002556 \leq T_0 \leq 0.2045$ and a phase angle range of $0.05 \leq \phi \leq 3.14$. All of the maneuvers have an initial radius $r_0 = 1.062716$ DU. The thin lines in Figure 6.12 are lines of constant time of flight, and the thicker lines running through the plot are bifurcation lines separating groups of control histories. Similar to Section 6.3.1, flight time increases as phase angle increases and initial thrust decreases. Also, $\partial^2 t_f / \partial \phi^2 < 0$, meaning changes in the phase angle have a smaller effect on flight time when the phase angle is large than when the angle is small.

We divide the solution space up into six groups. Groups A-E contain control time histories with a common sequence of sudden rotations. Like in Section 6.3.1,

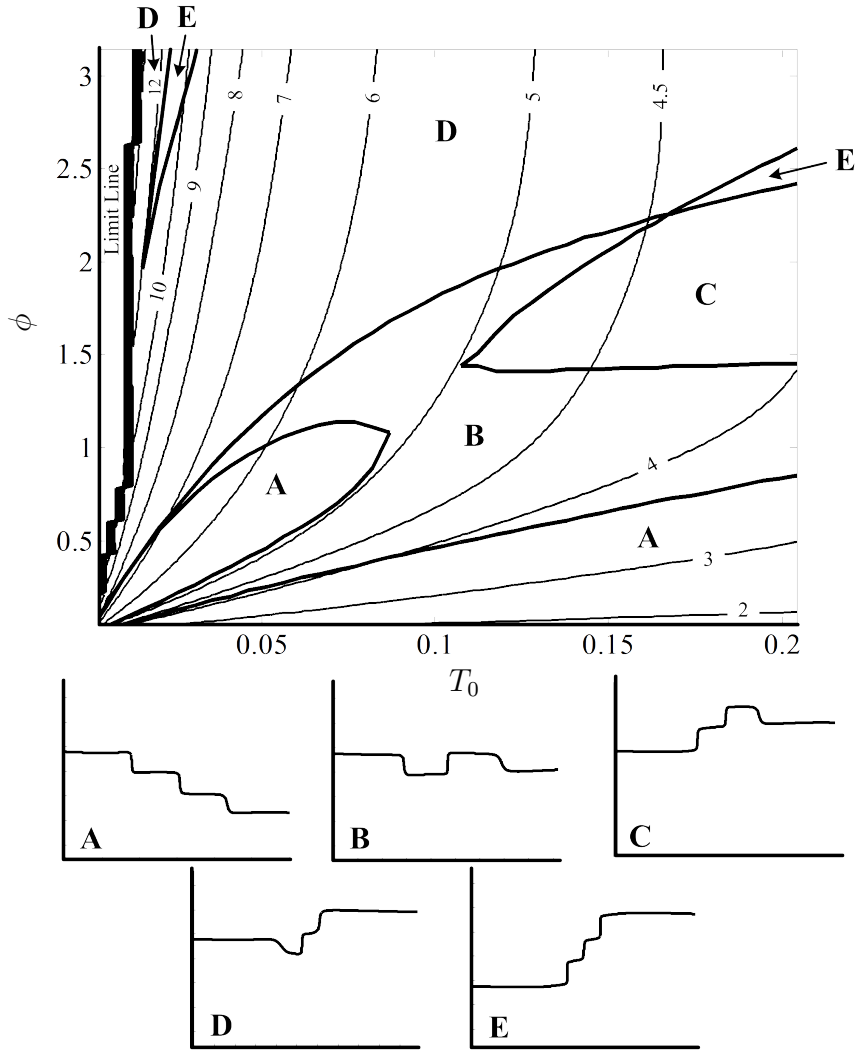

Figure 6.12: Control Angle Behavior and t_f Contour Plot for 3D Phasing Maneuvers

the bifurcation lines in Figure 6.12 separate sudden increases and sudden decreases of ψ. Since there are, at most, three sudden rotations in the control history, several up-down combinations are possible. Like in Section 6.3.1, the bifurcation lines fan out from the origin, forming sectors. At a low ϕ, the main sectors contain Groups A and B. Above those, the sectors alternate between Groups D and E. However, there are more lines present in the B sector that can end when they intersect with another line. The intersection closes off areas in the solution space to form pockets containing

Groups A and C. Lines can also cross to form other control sequences, such as Group E. We do not know why these intricate patterns occur.

Initial Sidereal Time

Figure 6.12 illustrates how t_f changes with respect to the input parameters, T_0 and ϕ; but in a tilted magnetic field there is one more input parameter, the initial sidereal time of the attracting body, L_0. The magnetic field vector at a fixed inertial point changes as the attracting body rotates so the initial time affects the optimal trajectory.

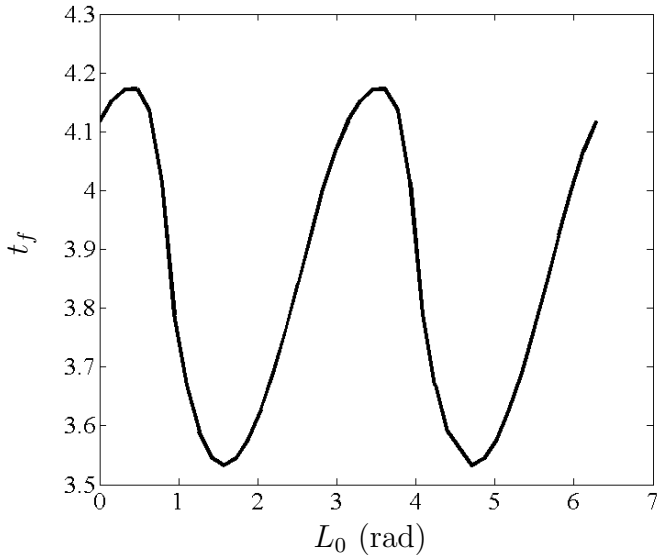

Figure 6.13: Time of Flight Vs. Initial Sidereal Time ($T_0 = 0.06134$, $\phi = 0.20$)

Figure 6.13 shows the time of flight as a function of the initial sidereal time. $L_0 = 0$ corresponds to the time when the magnetic dipole vector points in the positive x direction and is in the $\hat{\mathbf{n}}_1$-$\hat{\mathbf{n}}_3$ plane. The time of flight oscillates as L_0 varies and a minimum occurs at 4.59050 rad. Luckily, the sidereal time corresponding to the minimum time of flight is the same for all combinations of T_0 and ϕ we investigate.

6.3.3 Orbit Raising Maneuvers

We show contour plots of the solution space in Figures 6.14 and 6.15. Figure 6.14 has a thrust range of $0.001278 \leq T_0 \leq 0.2554$ and Figure 6.15 has a thrust range of $0.001278 \leq T_0 \leq 0.01532$. All of the maneuvers have an initial radius $r_1 = 1.062716$ DU. The solid lines are lines of constant time of flight in TUs while the dotted line separates two categories of control history types, Group A and Group B. As expected, the flight time decreases as T_0 increases and r_2 decreases. As with the phasing maneuvers, the benefit of increasing thrust to shorten the flight time decreases as thrust increases. However, unlike phasing maneuvers, $\partial^2 t_f / \partial r_2^2 > 0$. Small changes in r_2 have a larger effect on flight time when r_2 is large than when r_2 is small.

To illustrate the patterns in the optimal control, we divide Figure 6.14 into two groups. In Group A, $\bar{\psi}$ decreases when the control angle changes suddenly, and in Group B, $\bar{\psi}$ increases when the control angle changes suddenly. Group B contains only maneuvers which take less than one orbit to complete, while Group A contains both short-duration and multi-revolution maneuvers. The line separating the two groups is a bifurcation line, and control histories on either side of the line have the same behavior shown in Figure 6.10. The control plots for the two solutions on either side of the bifurcation line is nearly identical up to the sudden change in $\bar{\psi}$, and afterward the plots are separated by 360°. However, unlike the phasing maneuver solutions, there is only one bifurcation line in the optimal orbit-raising solution space.

As stated in Section 6.1.3, multi-revolution maneuvers can have several sudden decreases in $\bar{\psi}$. Figure 6.16 shows the changes in $\bar{\psi}$ as r_2 increases and $T_0 = 0.0013$. In the plots, the horizontal axis is time and the vertical axis is $\bar{\psi}$ where elapsed time for each frame is the time of flight, and the range of the optimal control angle is $-20° \leq \bar{\psi} \leq 20°$. This range of control angles shows that the EDT always thrusts in

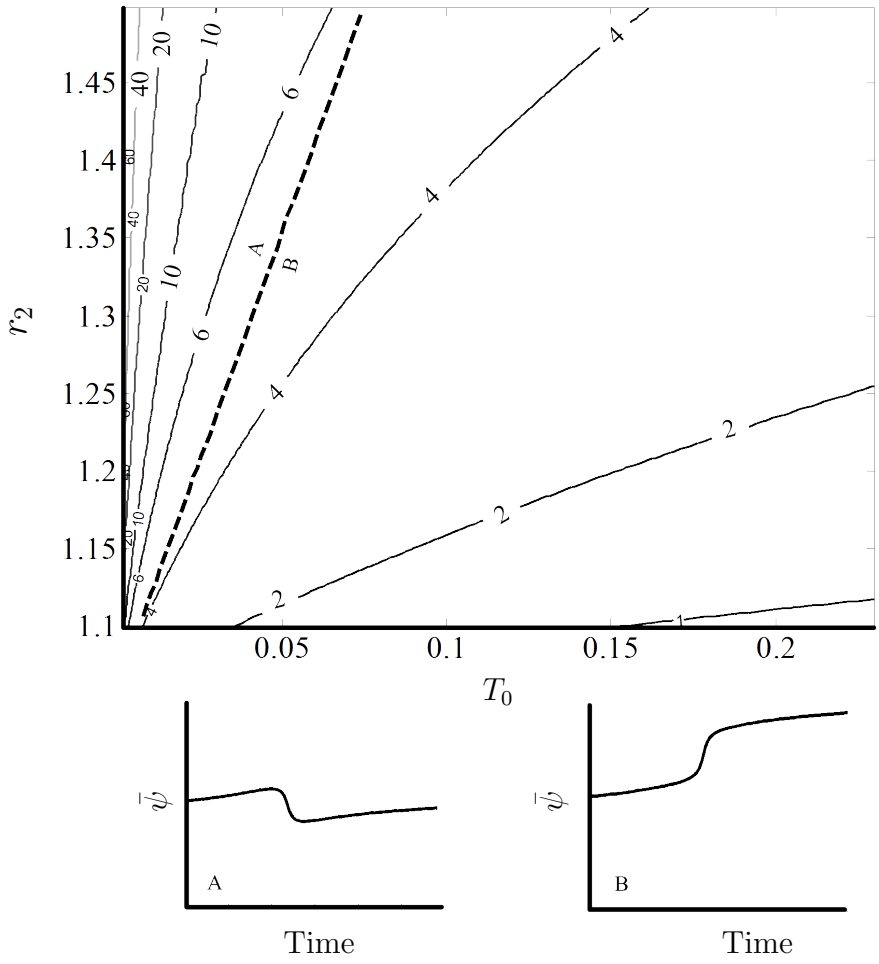

Figure 6.14: Control Angle Behavior and Time of Flight Contour Plot

the velocity direction. All of the frames look like sinusoidal waves, but the downward slopes are steeper than the upward slopes, keeping in line with the attributes of Group A. The amplitudes of the waves increase and decrease as r_2 increases, but overall, the amplitudes decrease as r_2 gets large. During each maneuver, however, the amplitude in the control oscillation increases as the EDT approaches its target orbit.

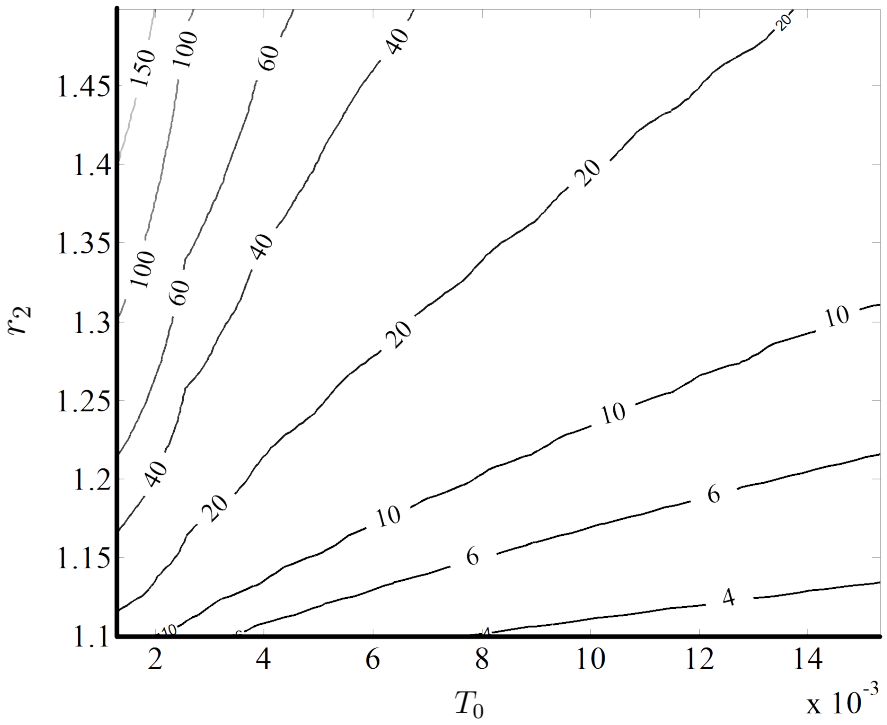

Figure 6.15: Control Angle Behavior and Time of Flight Contour Plot

6.4 Feasibility of Solutions

The feasibility of the solutions depends on the current limitations of an EDT, the size of the ionosphere, and the altitude above the attracting body. The main selling point for an EDT is that it does not require any propellant to generate thrust. The mass of the system must be low to make an EDT a viable option. Low mass means a thin tether diameter, which means the current in the wire must not be so high that the tether melts. The tether current in the TSS-1R experiment on the Space Shuttle reached 0.33 A, nearly three times higher than expected, and melted the tether.[2] Assuming thicker tethers will be built, the highest T_0 that can be achieved is about 0.10.

The size of the ionosphere determines the operating range of the EDT, which

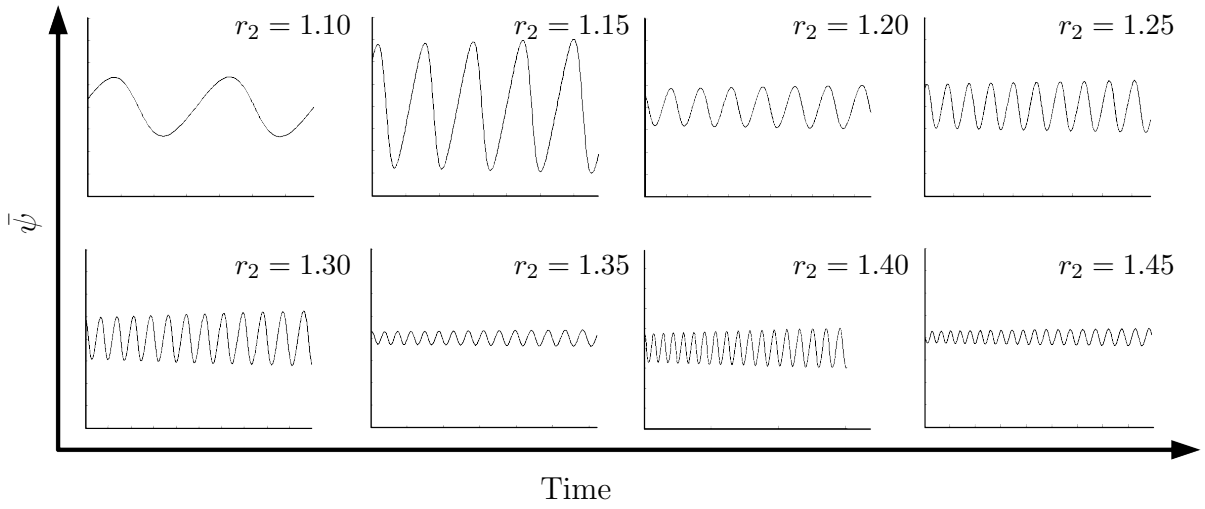

Figure 6.16: Control Angle vs. Time with $T_0 = 0.001278$ and Several r_2

cannot operate if it is not in a medium through which it can exchange electrons. For Earth, the ionosphere is about 3000 km thick, or extending to about 1.4 DU if 1 DU is equal to the earth's radius.

The last, most obvious limitation of the solutions is that they do not account for the size of the attracting body. Since 1 DU is the radius of the attracting body, any time the orbit radius is less than 1 DU, the EDT is in the attracting body. This occurs for high thrust phasing maneuvers, as seen in Figure 6.1. We require multi-stage optimization methods and constraints to keep the EDT above the attracting body's surface.

6.5 Validity of the Costate Differential Equation Approximation

In this section, we put the terms containing partial derivatives of B back into the costate differential equations. We compare solutions that use and do not use the

approximation and determine what effect the approximation has on the solution space of each maneuver.

Table 6.6: Approximate Solution Comparison for 2D Phasing Maneuvers

		Approximate Solution	**Optimal Solution**	% **Difference**
	λ_{y_0}	0.43944	0.43829	0.26437%
$\phi = 0.10$	$\lambda_{v_{x_0}}$	0.66727	0.65981	1.13097%
$T_0 = 0.010217$	$\lambda_{v_{y_0}}$	0.82752	0.81628	1.37672%
	t_f	5.16458	5.16458	0.000086769%
	λ_{y_0}	0.45439	0.43804	3.73327%
$\phi = 0.87$	$\lambda_{v_{x_0}}$	0.67501	0.60114	12.28892%
$T_0 = 0.12260$	$\lambda_{v_{y_0}}$	0.73722	0.64813	13.74485%
	t_f	4.11876	4.11810	0.016071%
	λ_{y_0}	-8.71033	-7.68712	13.31008%
$\phi = 0.01$	$\lambda_{v_{x_0}}$	0.12778	0.11708	9.14278%
$T_0 = 0.76370$	$\lambda_{v_{y_0}}$	-1.03100	-0.91019	13.27368%
	t_f	0.23608	0.23608	0.000176747%
	λ_{y_0}	0.33880	0.34640	2.19288%
$\phi = 1.49$	$\lambda_{v_{x_0}}$	0.66810	0.45323	47.40659%
$T_0 = 0.76370$	$\lambda_{v_{y_0}}$	0.26790	0.25072	6.85411%
	t_f	2.18831	2.17623	0.72191%

6.5.1 2D Phasing Maneuvers

Table 6.6 lists four cases that represent the accuracy of the costate differential equation approximation with respect to solutions that do not make the approximation. In all cases, the time of flight is estimated well. The largest deviation in the entire solution set for 2D phasing maneuvers is 0.722%. However, the initial costates are not as accurate. The initial costates in the optimal solution and the approximate solution differ by over 1% for low values of thrust and phase angle. For moderate to high values of thrust and lower phase angles, the initial costates for the two solutions vary between 3% and 14%, and for high thrust, high phase angle cases, $\lambda_{v_{x_0}}$ for the two solutions can vary by over 47%. Based on the numerical analysis described in

Chapter 5, the approximate solution is a good initial guess for the optimal solution for phase angles less than 0.50 rad, but Newton's method does not converge when the phase angle is higher.

One important observation is that the approximation does not change any of the trends in Section 6.3.1. Bifurcation lines separating alternating control categories are still present in the optimal solution space, and the near-invariance properties still hold. However, the approximation does shift the location of the bifurcation lines upward toward higher phase angles.

Table 6.7: Approximate Solution Comparison for 3D Phasing Maneuvers

		Approximate Solution	**Optimal Solution**	% **Difference**
	λ_{y_0}	0.38906	0.38577	0.85399%
	λ_{z_0}	0.26474	0.13486	96.30950%
$\phi = 2.20$	$\lambda_{v_{x_0}}$	0.50943	0.46854	8.72626%
$T_0 = 0.15325$	$\lambda_{v_{y_0}}$	1.00550	0.76771	30.97450%
	$\lambda_{v_{z_0}}$	-0.087798	-0.069271	26.74374%
	t_f	4.57942	4.57791	0.0033019%
	λ_{y_0}	-0.24286	-0.17349	39.98363%
	λ_{z_0}	1.77545	1.52714	16.25946%
$\phi = 0.10$	$\lambda_{v_{x_0}}$	0.82971	0.73557	12.79833%
$T_0 = 0.204334$	$\lambda_{v_{y_0}}$	-0.22433	-0.17796	26.05517%
	$\lambda_{v_{z_0}}$	-0.31525	-0.22549	39.80162%
	t_f	1.91593	1.91582	0.0060197%
	λ_{y_0}	0.34437	0.35030	1.69420%
	λ_{z_0}	0.41411	0.33677	22.96378%
$\phi = 0.90$	$\lambda_{v_{x_0}}$	0.48374	0.47002	2.91779%
$T_0 = 0.051084$	$\lambda_{v_{y_0}}$	1.06340	0.95857	10.93604%
	$\lambda_{v_{z_0}}$	-0.038356	-0.042823	10.42981%
	t_f	5.84843	5.84819	0.0041754%
	λ_{y_0}	0.038105	0.066544	42.73686%
	λ_{z_0}	0.23044	0.21143	8.98983%
$\phi = 0.63$	$\lambda_{v_{x_0}}$	0.10910	0.13337	18.19202%
$T_0 = 0.0076625$	$\lambda_{v_{y_0}}$	1.17982	1.15644	2.02207%
	$\lambda_{v_{z_0}}$	-0.0045737	-0.010968	58.29918%
	t_f	10.31206	10.31179	0.00267689%

6.5.2 3D Phasing Maneuvers

Table 6.7 shows cases that represent the accuracy of the approximate solutions for 3D phasing maneuvers. Similar to the 2D phasing maneuvers, the approximation accurately estimates the time of flight for 3D phasing maneuvers. However, the approximations for the initial costates are even less accurate for the 3D cases. As ϕ increases, the error in λ_{z_0}, $\lambda_{v_{y_0}}$, and $\lambda_{v_{z_0}}$ increases to near 100%. Also, the approximate solution does not make a good initial guess of the optimal solution unless $\phi < 0.15$.

As poor as the approximation is in estimating the initial values of the costates, the trends the approximation estimates in Section 6.3.2 are still present in the optimal solutions. There is still an intricate pattern of bifurcation lines separating five groups of control categories. Like the 2D phasing maneuver solutions, the bifurcations lines are shifted upward in the approximate solutions. Also the near-invariance properties still hold for the optimal solutions.

6.5.3 Orbit-Raising Maneuvers

The estimates of the initial costates and flight times for the optimal orbit-raising maneuvers are more accurate than the approximate solutions for phasing maneuvers. The difference between the flight times for both solutions is no more than 0.21%. The error in the initial costates increases as the target radius and initial thrust increases, but the error is no more than 50% in the entire solution space. However, all of the approximate solutions make atequate initial guesses for the optimal solution, which suggests the approximation is well within the radius of convergence for Newton's Method. Also, like the approximate solutions for the phasing maneuvers, the traits in Section 6.3.3 still hold for the optimal solutions.

Table 6.8: Approximate Solution Comparison for 2D Orbit-Raising Maneuvers

		Approximate Solution	**Optimal Solution**	% **Difference**
$r_2 = 1.100$	λ_{u_0}	0.039506	0.037055	6.61653%
$T_0 = 0.0012771$	λ_{v_0}	1.19977	1.20713	0.60963%
	t_f	13.72472	13.72460	0.000859996%
$r_2 = 1.498$	λ_{u_0}	0.048175	0.089962	46.44914%
$T_0 = 0.0012771$	λ_{v_0}	1.10766	1.11858	0.97627%
	t_f	206.63734	206.60598	0.015178%
$r_2 = 1.100$	λ_{u_0}	0.54377	0.55927	2.77077%
$T_0 = 0.076625$	λ_{v_0}	0.32702	0.33909	3.55935%
	t_f	1.39407	1.39407	0.0000818031%
$r_2 = 1.498$	λ_{u_0}	0.52161	0.56157	47.40659%
$T_0 = 0.076625$	λ_{v_0}	1.17364	1.42430	17.59888%
	t_f	5.57313	5.57196	0.020973%
$r_2 = 1.100$	λ_{u_0}	0.35011	0.36171	3.20680%
$T_0 = 0.25542$	λ_{v_0}	0.11489	0.11966	3.98578%
	t_f	0.77742	0.77742	0.000035182%
$r_2 = 1.498$	λ_{u_0}	0.66403	0.83825	20.78319%
$T_0 = 0.25542$	λ_{v_0}	0.70358	0.96561	27.13639%
	t_f	3.25854	3.25807	0.014526%

6.6 Summary

In this section, we present numerical solutions for the optimal control of EDT maneuvers. We compare optimal solutions for an EDT to that of a constant-thrust spacecraft. An EDT performing a phasing maneuver reaches its target faster than a constant-current spacecraft in all cases when the magnetic field is not tilted and in some cases, when the phase angle is high enough, when the magnetic field is tilted. Also, an EDT performing a phasing maneuver has the same invariance properties as a constant-thrust spacecraft.

In all cases, an EDT performs an orbit-raising maneuver slower than a constant-thrust spacecraft because the strength of the magnetic field decreases as orbit radius increases. However, the initial costates for an EDT performing an orbit-raising ma-

neuver have no invariance properties.

One common trait in all of the solutions is that each solution space contains bifurcations. Phasing maneuvers have multiple bifurcation lines in the solution space while orbit-raising maneuvers only have one in the range of parameters investigated. Lastly, we present the feasibility and validity of the solutions. The costate differential equation approximation is not good in estimating the initial costates but is good in estimating the flight times of all three maneuvers. Also, none of the solution space traits change in the optimal solution spaces. In the last chapter, we summarize all of our results, present our conclusions, and offer suggestions on how to continue our research.

Chapter 7

Conclusions

We develop the optimal equation of motion in two and three dimensions and in Cartesian and polar coordinates using Pontryagin's Minimum Principle and the Legendre-Clebsch condition. We set up the problem by defining boundary conditions for each of the three maneuvers: a phasing maneuver in the equatorial plane of a non-tilted magnetic field, an equatorial plane phasing maneuver in a tilted magnetic field, and an orbit-raising maneuver in the equatorial plane of a non-tilted magnetic field. Our solution algorithm uses Adaptive Simulated Annealing, a global, stochastic optimization method, to reduce the large search space for solutions to a small area containing the global minimum. Newton's method then reduces the error in the residual to below a specified tolerance. Once we find one solution, we find many more using numerical continuation.

We give sample solutions for each of the maneuvers. To complete a 2D phasing maneuver, the EDT thrusts inward toward the attracting body to lower the altitude, rotates suddenly midway through the maneuver, and thrusts outward to meet with the target spacecraft. A 3D phasing maneuver follows the same sequence of events; however, the EDT can rotate suddenly up to three times. In general, the EDT must

also thrust out-of-plane because the magnetic field vector is not perpendicular to the orbit plane. To complete a 2D orbit-raising maneuver, the EDT thrust vector oscillates near the velocity direction during the whole transfer. The thrust vector oscillates once per orbit, and if the maneuver takes longer than one orbit, the downward slope of the oscillation is always steeper than the upward slope.

We compare EDT solutions with constant-thrust solutions found in the literature. In all cases, an EDT performed a phasing maneuver in a non-tilted magnetic field faster than a constant-thrust spacecraft. This is because the EDT lowers its altitude to catch up to its target. Decreasing the orbit radius increases the magnitude of the magnetic field vector which increases the thrust. An EDT performing a phasing maneuver in a tilted magnetic field is faster than a constant-thrust spacecraft only when the phase angle is large and the EDT can use its thrust advantage. If the phase angle is small, the out-of-plane motion causes the EDT to be slower. An EDT performing an orbit-raising maneuver is always slower than a constant-thrust spacecraft because thrust decreases as orbit radius increases.

The solution spaces for each of the maneuvers contain bifurcation lines which separate groups of solutions with a common optimal control time history. Control histories for solutions on either side of the line have sudden rotations in opposite directions, but the magnitude of the rotation is identical. In general, the bifurcation lines extend out from the origin of the T_0-ϕ plane. The orbit-raising solution space has only one bifurcation line while the phasing maneuver solution spaces have several. The 3D phasing maneuver solution space also has secondary bifurcation lines which intersect each other and the main lines to form an intricate pattern. Overall, the solution spaces give a "big-picture" view of the optimal performance for a point-mass electrodynamic tether.

There is no limitation to how far EDT optimal control reach can go. The purpose

of this study is to provide a base of solutions to build from. One possible extension of this work is to apply the tilted dipole magnetic field model to orbit-raising maneuvers. From there, a future researcher can find phasing and orbit-raising solutions for different inclination orbit planes. The magnetic field vector varies more in higher inclinations, and the solutions could present some interesting results. When the inclination is no longer zero, the departure time becomes more important. It is possible that beginning the maneuver at different points in the orbit can reduce the flight time. Solutions for non-circular orbits could prove interesting as well. After possibilities for point mass solutions are exhausted, a future researcher could find all of the same solutions for a tether with a different dynamical model.

Bibliography

[1] Kim, M., *Continuous Low-Thrust Trajectory Optimization: Techniques and Applications*, Ph.D. thesis, Virginia Tech, Blacksburg, VA, 2005.

[2] Cosmo, M. L. and Lorenzini, E. C., editors, *Tethers in Space Handbook*, Smithsonian Astrophysical Observatory, 1997.

[3] Chi, C.-H., *Survey of PDP Data from PMG Delta II*, Master's thesis, Naval Postgraduate School, Monterey, CA, 1995.

[4] Cliff, E. M., "Trajectory Optimization Techniques Lecture Notes," Virginia Tech, Blacksburg, VA, 2008.

[5] Bryson, A. E. and Ho, Y.-C., *Applied Optimal Control: Optimization, Estimation, and Control*, Hemisphere Publishers, New York, 1981.

[6] Wiesel, W. E. and Alfano, S., "Optimal Many-Revolution Orbit Transfer," *Journal of Guidance, Control, and Dynamics*, Vol. 8, No. 1, 1985, pp. 155–157.

[7] Alfano, S. and Thorne, J. D., "Circle-to-Circle Constant-Thrust Orbit Raising," *Journal of the Astronautical Sciences*, Vol. 42, No. 1, 1994, pp. 35–45.

[8] Thorne, J. D. and Hall, C. D., "Approximate Initial Lagrange Costates for Continuous-Thrust Spacecraft," *Journal of Guidance, Control, and Dynamics*, Vol. 19, No. 2, 1996, pp. 913–922.

[9] Thorne, J. D. and Hall, C. D., "Minimum-Time Continuous-Thrust Orbit Transfers," *The Journal of the Astronautical Sciences*, Vol. 45, No. 4, 1997, pp. 411–432.

[10] Thorne, J. D., *Optimal Continuous-Thrust Orbit Transfers*, Ph.D. thesis, Air Force Institute of Technology, 1996.

[11] Hall, C. D. and Collazo-Perez, V., "Minimum-time Orbital Phasing Maneuvers," *Journal of Guidance, Control, and Dynamics*, Vol. 26, No. 6, 2003, pp. 934–941.

[12] Beletsky, V. V. and Levin, E. M., *Dynamics of Space Tether Systems (Advances in the Astronautical Sciences)*, Univelt, Inc., San Diego, 1993.

[13] Tragesser, S. G. and San, H., "Orbital Maneuvering with Electrodynamic Tethers," *Journal of Guidance, Control, and Dynamics*, Vol. 25, No. 2, 2003, pp. 805–810.

[14] Pearson, J., Levin, E., Carroll, J. A., and Oldson, J. C., "Orbital Maneuvering with Spinning Electrodynamic Tethers," 2nd International Energy Conversion Engineering Conference, Providence, RI, 2004.

[15] Williams, P., Watanabe, T., Blanksby, C., Trivailo, P., and Fujii, H. A., "Libration Control of Flexible Tethers Using Electromagnetic Forces and Movable Attachment," *Journal of Guidance, Control, and Dynamics*, Vol. 27, No. 5, 2004, pp. 882–897.

[16] Pelaez, J. and Andres, Y. N., "Dynamic Stability of Electrodynamic Tethers in Inclined Elliptical Orbits," *Journal of Guidance, Control, and Dynamics*, Vol. 28, No. 4, 2005, pp. 611–622.

[17] Pelaez, J. and Lorenzini, E. C., "Libration Control of Electrodynamic Tethers in Inclined Orbits," *Journal of Guidance, Control, and Dynamics*, Vol. 28, No. 2, 2005, pp. 269–279.

[18] Ellis, J. R. and Hall, C. D., "Dynamics of an Electrodynamic Tether System Containing Gyrostat End Bodies," 17th Annual Space Flight Mechanics Meeting. Sedona, AZ, January 28 - February 1, 2007.

[19] Ellis, J. R. and Hall, C. D., "Numerical Model Development and Verification for the Dynamics of an Electrodynamic Tether System," AAS/AIAA Space Flight Mechanics Meeting. Galeston, TX, January 27-31, 2008.

[20] Williams, P., "Optimal Orbital Transfer with Electrodynamic Tethers," *Journal of Guidance, Control, and Dynamics*, Vol. 28, No. 2, 2005, pp. 369–372.

[21] Stevens, R. and Wiesel, W., "Large Time Scale Optimal Control of an Electrodynamic Tether Satellite," *Journal of Guidance, Control, and Dynamics*, Vol. 31, No. 6, 2008, pp. 1716–1727.

[22] Makovec, K. L., *A Nonlinear Magnetic Controller for Three-Axis Stability of Nanosatellites*, Master's thesis, Virginia Tech, Blacksburg, VA, 2001.

[23] Cliff, E. M., "Notes for Matt Bitzer," Virginia Tech, Blacksburg, VA, 2009.